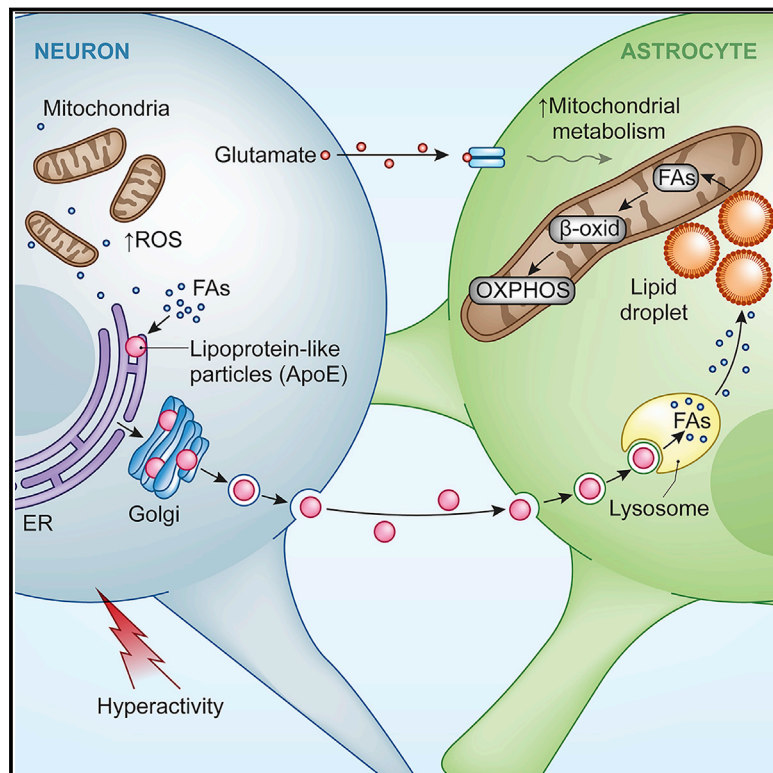# Cell

Neuron-Astrocyte Metabolic Coupling Protects against Activity-Induced Fatty Acid Toxicity

Graphical Abstract

Authors

Maria S. Ioannou, Jesse Jackson,
Shu-Hsien Sheu, ..., Harald F. Hess,
Jennifer Lippincott-Schwartz, Zhe Liu

Correspondence

ioannou@ualberta.ca (M.S.I.),
lippincottschwartzj@janelia.hhmi.org
(J.L.-S.),
liuz11@janelia.hhmi.org (Z.L.)

In Brief

Hyperactive neurons produce toxic fatty
acids that are transferred via lipid
particles to astrocytes where these fatty
acids are detoxified as a means of
protecting neurons during periods of
enhanced activity.

Highlights

- Hyperactive neurons release excess FAs in lipid particles associated with ApoE

- Astrocytes endocytose neuron-derived lipid particles, delivering the FAs to LDs

- Astrocytes with LDs upregulate metabolic and detoxification genes

- Neural activity triggers astrocytic consumption of FAs by mitochondrial oxidation

CellPress

Neuron-Astrocyte Metabolic Coupling Protects against Activity-Induced Fatty Acid Toxicity

Maria S. Ioannou,[1,*] Jesse Jackson,[2,3] Shu-Hsien Sheu,[1] Chi-Lun Chang,[1] Aubrey V. Weigel,[1] Hui Liu,[1] H. Amalia Pasolli,[1] C. Shan Xu,[1] Song Pang,[1] Doreen Matthies,[1] Harald F. Hess,[1] Jennifer Lippincott-Schwartz,[1,*] and Zhe Liu[1,4,*]

[1]Janelia Research Campus, Howard Hughes Medical Institute, Ashburn, VA 20147, USA
[2]Department of Physiology, University of Alberta, Edmonton, AB T6G 2H7, Canada
[3]Neuroscience and Mental Health Institute, Edmonton, AB T6G 2E1, Canada
[4]Lead Contact
*Correspondence: ioannou@ualberta.ca (M.S.I.), lippincottschwartzj@janelia.hhmi.org (J.L.-S.), liuz11@janelia.hhmi.org (Z.L.)
https://doi.org/10.1016/j.cell.2019.04.001

SUMMARY

Metabolic coordination between neurons and astrocytes is critical for the health of the brain. However, neuron-astrocyte coupling of lipid metabolism, particularly in response to neural activity, remains largely uncharacterized. Here, we demonstrate that toxic fatty acids (FAs) produced in hyperactive neurons are transferred to astrocytic lipid droplets by ApoE-positive lipid particles. Astrocytes consume the FAs stored in lipid droplets via mitochondrial β-oxidation in response to neuronal activity and turn on a detoxification gene expression program. Our findings reveal that FA metabolism is coupled in neurons and astrocytes to protect neurons from FA toxicity during periods of enhanced activity. This coordinated mechanism for metabolizing FAs could underlie both homeostasis and a variety of disease states of the brain.

INTRODUCTION

Neurons and astrocytes operate as a tightly coupled unit for energy metabolism in the brain. While neurons expend a considerable amount of ATP on neurotransmission, astrocytes provide neurons with metabolic substrates and antioxidants (Bélanger et al., 2011; Bélanger and Magistretti, 2009). This metabolic support allows neurons to allocate more cellular resources to sustain high activity rates during information processing.

An important area in neuron-astrocyte interaction relates to the metabolism of fatty acids (FAs). FAs are components of phospholipids in cellular membranes and are stored within cells as energy-rich triacylglycerides localized in lipid droplets (LDs). Storage of FAs in LDs serves two purposes. First, it removes excess free FAs from the cytoplasm, which are toxic and disrupt mitochondrial membrane integrity (Unger et al., 2010; Nguyen et al., 2017). Second, LDs deliver FAs into mitochondria for their consumption as an alternative energy source during periods of nutrient depletion (Rambold et al., 2015). Interestingly, neurons do not typically make LDs and have a low capacity for FA consumption in mitochondria for energy production (Schönfeld and Reiser, 2013). This makes neurons particularly sensitive to

periods of enhanced activity, in which high levels of reactive oxygen species (ROS) induce peroxidation of FAs (Reynolds and Hastings, 1995). Unless they can destroy or remove these peroxidated FAs, highly active neurons will undergo pathophysiology, giving rise to neurodegeneration (Sultana et al., 2013).

Unlike neurons, astrocytes make LDs and produce many anti-oxidants, allowing them to effectively manage oxidative stress (Bélanger and Magistretti, 2009). Given the tight coordination between neurons and astrocytes, the question arises as to whether astrocytes help highly active neurons avoid FA toxicity by taking up excess FAs from neurons and storing them in LDs. In fact, oxidative stress in neurons triggers LD formation in neighboring astrocytes (Liu et al., 2015; Bailey et al., 2015), and this is dependent on the presence of apolipoproteins (Liu et al., 2017). This suggests that active neurons transfer their damaged FAs to astrocytes via lipoprotein particles, but how this occurs and how astrocytes respond to this transfer have not been characterized.

Here, we investigate the cellular mechanisms of neuron-astrocyte metabolic coupling that protects neurons from FA toxicity during periods of enhanced activity. We first demonstrate that hyperactive neurons accumulate FAs, including peroxidated lipids. Rather than storing these toxic FAs in LDs, we show that neurons expel them in association with ApoE-positive lipid particles. Nearby astrocytes then endocytose these particles and incorporate the FAs in LDs. We also report that astrocytes respond to increased neuronal activity by enhancing breakdown of LDs and feeding liberated FAs into the mitochondria as fuel for oxidative phosphorylation. During this process, astrocytes upregulate genes involved in neutralizing oxidative species, as well as genes involved in energy metabolism. Astrocytes thus protect the brain by taking up FAs released from neurons and switching on genes for oxidant detoxification and FA-based oxidative energy metabolism. The activity-dependent stimulation of lipid metabolism in astrocytes provides a program for avoiding FA toxicity in response to the fluctuating needs of neurons.

RESULTS

Effect of Excitotoxicity on the Systems that Regulate FA Trafficking in Neurons

To explore the trafficking itinerary of FAs in highly active neurons, we stimulated cultured hippocampal neurons with
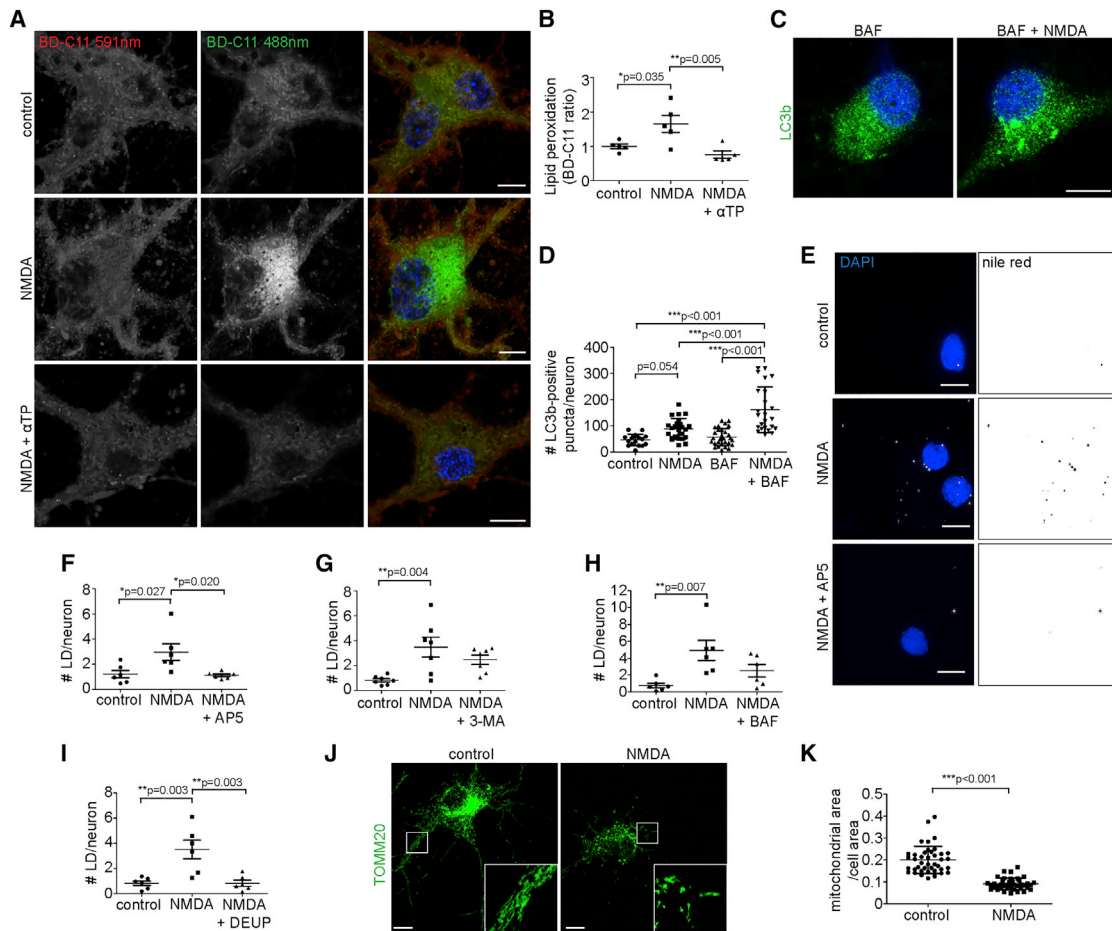
Figure 1. Excitotoxicity as an Oxidative Stress in Neurons

(A and B) Cropped confocal images of neurons ± NMDA and α-tocopherol (αTP) were labeled with BD-C11. Red (591 nm) and green (488 nm) show total and peroxidated lipids, respectively. 3 independent experiments; n = 5 coverslips/treatment; 24.7±6.9 cells/coverslip; mean ± SEM.

(C and D) Cropped confocal images of neurons ± NMDA and BAF immunostained for LC3b. 2 independent experiments; n = 3 coverslips/treatment; 15.7 ± 7.0 cells/coverslip; mean ± SEM.

(E and F) Neurons ± NMDA and AP5 were fixed, stained with Nile Red, and the number of LDs was quantified. Left panel: Cropped widefield images of LDs displayed as maximum intensity projections on top of single DAPI image. Right panel: Inverted maximum intensity projection of LDs. 5 independent experiments; n = 6 coverslips/treatment; 26.4 ± 5.9 cells/coverslip; mean ± SEM.

(G) Neurons ± NMDA and 3-MA were fixed, stained with BD493, and the number of LDs were quantified. 4 independent experiments; n = 7 coverslips/treatment; 25.2 ± 4.5 cells/coverslip; mean ± SEM.

(H) Neurons ± NMDA and BAF were fixed, stained with BD493, and the number of LDs were quantified. 3 independent experiments; n = 6 coverslips/treatment; 33.8 ± 7.4 cells/coverslip; mean ± SEM.

(I) Neurons ± NMDA and DEUP were fixed, stained with BD493, and the number of LDs were quantified. 3 independent experiments; n = 6 coverslips/treatment; 30.5 ± 4.2 cells/coverslip mean ± SEM.

(J and K) Cropped confocal images of neurons ± NMDA were immunostained for TOMM20. Blind quanfitifaction of mitochondrial area. 2 independent experiments; n = 60 cells/treatment; mean ± SD.

Scale bars are 10 μm. See Figure S1.

N-methyl-D-aspartate (NMDA) to induce excitotoxicity. Specifically, NMDA treatment is predicted to trigger lipid and FA peroxidation (Haba et al., 1991; Parihar and Hemnani, 2004), leading neurons to respond through potential changes in autophagy, LD biogenesis and mitochondrial morphology. We first assessed whether lipids undergo peroxidation following NMDA treatment using the BODIPY 581/591 C11 (BD-C11) ratiometric lipid peroxidation sensor. Following peroxidation, BD-C11 shifts its fluorescence emission peak from 590 (red) to 510 (green) nm. We

observed an increase in the BD-C11 ratio (green to red) in neurons treated with NMDA, indicating increased lipid peroxidation, that was prevented by the addition of the lipid soluble antioxidant α-tocopherol (Figures 1A and 1B). We next incubated neurons with linoleamide alkyne (LAA), which incorporates into cellular membranes. Upon lipid peroxidation, reactive aldehydes are produced, which modify proteins that can be detected using Alexa Fluor 488-conjugated Click-iT chemistry (Figure S1A). We observed increased Alexa Fluor 488 fluorescence in neurons

following NMDA treatment compared to control cells (Figures S1B–S1D), further supporting the view that excitotoxicity through NMDA treatment increases neuronal lipid peroxidation.

Once neurons have exhausted their capacity to quench peroxidated lipids with antioxidants (Seiler et al., 2008), we reasoned that they would need a mechanism to remove damaged membranes. One way is through autophagy; the process whereby portions of an organelle or membrane are broken down in the lysosome. We therefore tested whether excitotoxicity through NMDA treatment caused an increase in autophagy in our hippocampal neurons using the autophagy marker LC3. This was accomplished using bafilomycin to prevent autophagosome fusion with lysosomes (Redmann et al., 2017), thereby allowing autophagosomes to accumulate within cells. When neurons were stimulated with NMDA in the presence of bafilomycin, increased levels of the LC3b were detected, indicating that excitotoxicity enhances neuronal autophagy (Figures 1C and 1D). This result suggests that peroxidated lipids in membranes of excited neurons are mobilized by autophagy for eventual removal from these cells.

Peroxidated lipids delivered to lysosomes through autophagy are expected to be broken down into FAs, which can quickly leak into the cytoplasm. To avoid FA toxicity from FA accumulation in the cytoplasm, autophagy-mobilized FAs in non-neuronal cells are delivered to LDs, increasing their number (Unger et al., 2010; Rambold et al., 2015). We tested, therefore, whether LDs were induced in NMDA-treated neurons. We first confirmed that neurons could form LDs by incubating with oleic acid, an 18-carbon monounsaturated FA, or linoleic acid, an 18-carbon polyunsaturated FA. An accumulation of LDs was seen with both types of FAs (Figures S1E and S1F). Next, we tested whether neurons form LDs in response to NMDA-induced excitotoxicity. A modest but significant increase in the number of LDs was observed (Figures 1E–1I, S1G, and S1H), which could be prevented with the NMDA receptor antagonist AP5 (Figures 1E and 1F).

Autophagy was responsible for this increase in LD formation following neuronal excitotoxicity since NMDA-induced LD formation was reduced by blocking autophagosome formation using 3-methyladenine (3-MA) (Figure 1G) or by inhibiting lysosomal autophagosome degradation using bafilomycin (Figure 1H). We also observed a reduction in NMDA-induced LD formation in the presence of the pan-lipase inhibitor diethylumbelliferyl phosphate (DEUP) (Figure 1I), which taken together with involvement of autophagy points to the role of lysosomal lipases in the LD formation. Collectively, these data suggested that, following excitotoxicity, neurons generate excess FAs by autophagy and some of these FAs are stored in a small number of LDs.

We wondered why there were not more LDs forming in cells undergoing NMDA treatment. One possibility is that FAs are being efficiently delivered from LDs to mitochondria and broken down by mitochondrial β-oxidation (Rambold et al., 2015). However, prior work has shown that neurons have a low capacity for FA degradation in mitochondria (Schönfeld and Reiser, 2017). Moreover, to efficiently degrade FAs, the mitochondrial network would have to be extensively fused (Rambold et al., 2015). We examined, therefore, mitochondrial morphology and area in control neurons and neurons treated with NMDA to evaluate mitochondrial capacity to degrade FAs. Rather than being extensively fused, the mitochondria in NMDA-treated neurons were highly fragmented (Figures 1J and S1I) (Nguyen et al., 2011). Additionally, there was a decrease in mitochondrial area in neurons treated with NMDA (Figure 1K), suggesting mitochondria were being consumed by the increased autophagy occurring in these cells. Consistent with the remaining fragmented mitochondria being unable to consume FAs, we preloaded neurons with BODIPY 558/568 C12 (Red-C12), a fluorescently labeled, saturated FA analog (Rambold et al., 2015; Wang et al., 2010), and were unable to detect the labeled FAs in the mitochondria following NMDA treatment (Figure S1J). Based on these results, we concluded that excess, free FAs generated by autophagy in neurons treated with NMDA were not being turned over within mitochondria. Rather, some other pathway was removing these FAs from neurons to avoid FA toxicity.

Highly Active Neurons Release FAs in Dense Carriers

In non-neuronal cells containing highly fragmented mitochondria, FAs are expulsed and taken up by neighboring cells (Rambold et al., 2015). We thus tested whether FAs in neurons could be released and taken up by neighboring astrocytes. To do so, we developed a transfer assay to monitor FA trafficking from neurons to astrocytes using Red-C12 (Rambold et al., 2015; Wang et al., 2010). We first incubated neurons with trace amounts of Red-C12 overnight and then co-cultured the labeled neurons with astrocytes on different coverslips separated by paraffin wax (Figure 2A). We found that fluorescently labeled FAs in neurons are transferred to GFAP-positive astrocytes in the absence of cell contact and that these FAs accumulate in LDs (Figures 2A, 2B, S2A, and S2B). To exclude the possibility that contaminating astrocytes in our neuronal cultures were responsible for transferring the FAs, we performed transfer assays with neuronal cultures grown in AraC to eliminate proliferating glial cells. We found that neuronal cultures with over 98% purity transferred labeled FAs to astrocytes (Figures S2C–S2F). Interestingly, the amount of FA transfer from neurons to astrocytes was higher than from astrocytes to astrocytes showing specificity of transfer and providing further evidence that contaminating astrocytes are not involved (Figure S2G). No appearance of Red-C12-positive LDs was observed when the transfer assay was performed with co-cultured neurons (Figure S2G). Therefore, neurons transfer FAs preferably to neighboring astrocytes. Since hyperactivity induces lipid peroxidation in neurons (Figure 1), we next examined whether neurons release peroxidated lipids. This was achieved by extracting lipid hydroperoxides from the media and reacting them with ferrous ions to produce ferric ions that were then detected using thiocyanate ions as a chromogen. We detected lipid hydroperoxides in neuron-conditioned medium at steady state, and the level of lipid hydroperoxides was increased upon NMDA treatment (Figure 2C). Altogether, these data show that neurons transfer lipids, including those damaged by peroxidation to astrocytes.

We next sought to determine the mechanism of this FA transfer. We took advantage of differential centrifugation to deplete various components from the media of neurons labeled with Red-C12 (Figure 2D). We found that following low-speed centrifugation to remove dead cells and debris, neuron-conditioned media continued to supply labeled FAs to astrocytic LDs
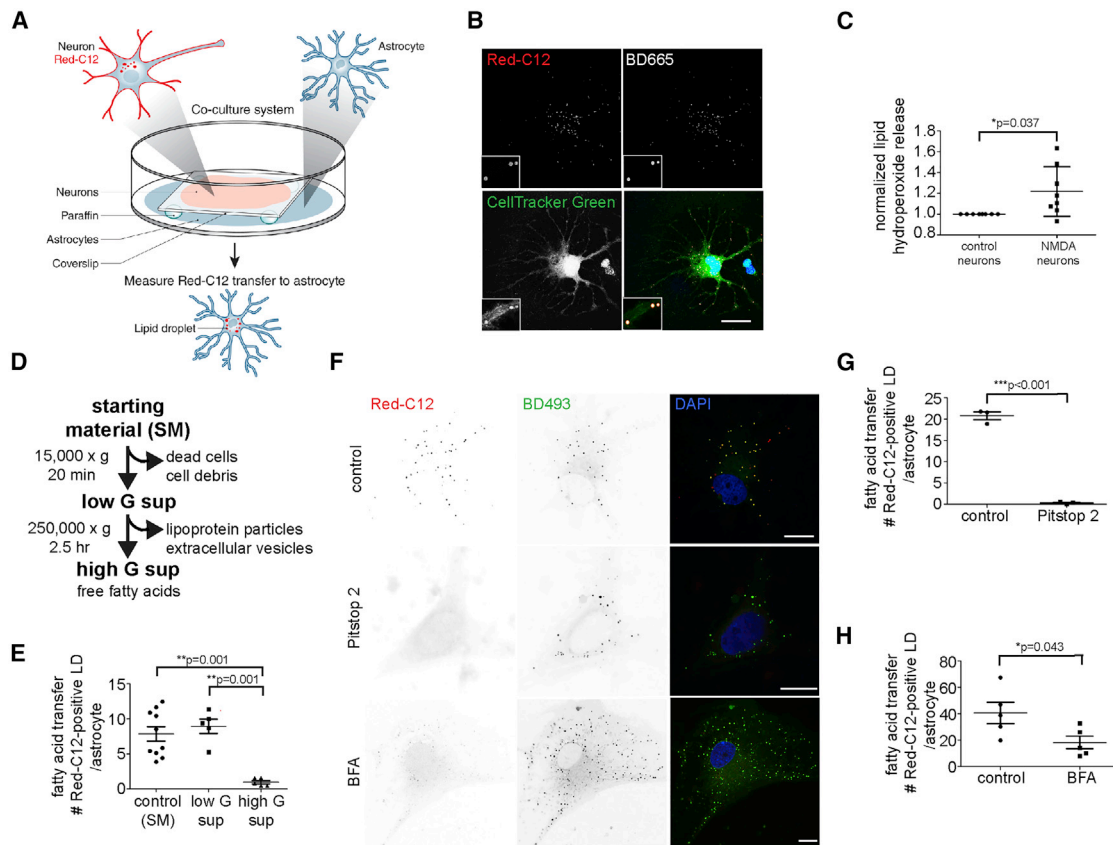
Figure 2. Neurons Transfer FA to Astrocytes

(A) Schematic of Red-C12 transfer assay.

(B) Cropped confocal image of astrocytes post-transfer assay. Cells were stained with CellTracker Green were analyzed for Red-C12 in LDs labeled with BD665.

(C) Neuron-conditioned media analyzed for lipid hydroperoxides. NMDA-treated neurons normalized to control neurons. 3 independent experiments; n = 8 per treatment; mean ± SD.

(D) Schematic of centrifugation assay. Supernatant (sup).

(E) Quantification of Red-C12-positive LDs in astrocytes treated with neuron-conditioned media following centrifugation. 3 independent experiments; minimum of n = 5 coverslips/treatment; 23.5 ± 10.0 cells/coverslip; mean ± SEM.

(F) Cropped confocal image of astrocytes following transfer assay ± DMSO, Pitstop 2 or Brefeldin A (BFA). Cells were fixed and stained with BD493 to label LDs. Scale bars are 10 μm.

(G and H) Quantification of (F). Pitstop 2: 2 independent experiments; n = 3 coverslips/treatment. 23.5 ± 3.5 cells/coverslip; mean ± SEM. BFA: four independent experiments; n = 6 coverslips/treatment. 27.5 ± 3.9 cells; mean ± SEM.

All images are maximum intensity projections are shown. Scale bars are 10 μm. See Figure S2.

(Figure 2E). Consistent with this, we observed that astrocytic LDs were labeled with Red-C12 following incubation with 0.2 μm pore filtered neuron-conditioned media (Figure S2H). These results suggested that FAs are being transferred as free FAs or as small dense carriers such as lipoprotein particles from neurons to astrocytes.

Following high-speed centrifugation to remove small dense carriers, the transfer of labeled FAs from neuron-conditioned media to astrocytes was eliminated (Figures 2E and S2I). As free FAs such as oleic acid-BSA remain in the supernatant following high-speed centrifugation (Figure S2J), these data pointed to small dense carriers as the vehicle for FA transfer. Consistent with this model, FA transfer to astrocytes was blocked by inhibiting endocytosis with Pitstop 2, suggesting that internalization of small dense carriers by astrocytes is required for the transfer (Figures 2F and 2G). FA transfer is unlikely mediated by exosomes as addition of the exosome inhibitor GW4869 (Trajkovic et al., 2008) had no effect in our transfer assay (Figure S2K). However, transfer of FAs was reduced by the addition of brefeldin A (BFA), a fungal metabolite that blocks export from the endoplasmic reticulum (ER) into the secretory pathway (Klausner et al., 1992) (Figures 2F and 2H). As BFA does not block endocytosis (Lippincott-Schwartz et al., 1991), this suggested that neuronal FA release through small dense carriers is dependent on the secretory pathway.

Astrocytes Internalize FAs Secreted by Neurons in Lipoprotein Particles

ApoE, a component of high-density lipoprotein (HDL)-like particles in the nervous system (Pitas et al., 1987), is required for
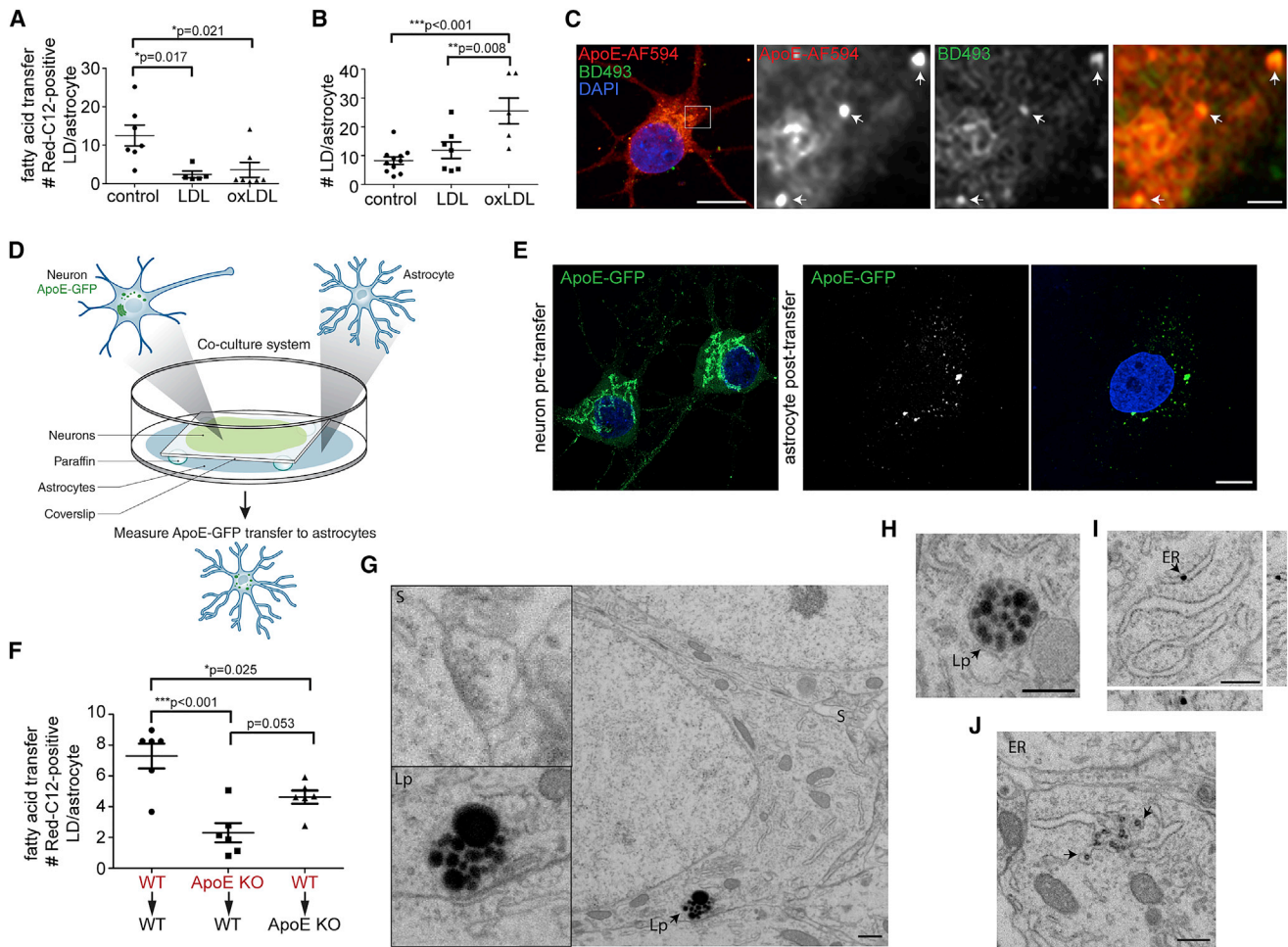
Figure 3. Neurons Transfer FAs by ApoE-Positive Lipid Particles

(A) Quantification of Red-C12-positive LDs in astrocytes following transfer assay ± LDL or oxLDL. 3 independent experiments; minimum of n = 5 coverslips/treatment; 18.2 ± 3.4 cells; mean ± SEM.

(B) Astrocytes ± LDL or oxLDL were fixed, stained with BD493 and the number of LDs were quantified. 3 independent experiments; minimum of n = 6 coverslips/treatment. 23.7 ± 4.3 cells/coverslip; mean ± SEM.

(C) Cropped confocal image of neurons were immunostained for ApoE and stained with BD493. Boxed area magnified in right panels. Arrows highlight co-localization. Scale bars are 10 and 1 μm.

(D) Schematic of ApoE transfer assay.

(E) Left panel: Cropped confocal image of neurons expressing ApoE-GFP pre-transfer. Right panel: Cropped confocal image showing the appearance of ApoE-GFP in astrocytes post-transfer. Scale bars are 10 μm.

(F) Quantification of Red-C12-positive LDs in astrocytes following transfer assay using ApoE knockout (KO) or wild-type (WT) cells. 3 independent experiments; n = 6 coverslips/treatment; 27.6 ± 7.5 cells/coverslip; mean ± SEM.

(G–J) Pyramidal neuron from CA1 imaged by FIB-SEM. Lp, lipid particles, magnified on right. S, synapse. ER, lipid-dense structure in lumen of the ER. Orthogonal view of ER structure included.

Scale bars are 500 nm. See Video S1 and Figure S3.

astrocytic LD accumulation in response to oxidative stress (Liu et al., 2017). To test the hypothesis that lipoprotein particles might mediate transfer of FAs from neurons to astrocytes, we added excess purified low-density lipoprotein (LDL) or oxidatively modified oxLDL in a pulse-chase assay to competitively block lipoprotein particles receptors on astrocytes. We found that incubation with LDL or oxLDL dramatically reduced Red-C12 transfer from neurons to astrocytes (Figure 3A), indicating that internalization of lipoprotein particles is important for astro-

cytes to receive FAs. Furthermore, astrocytes increase LD number when treated with oxLDL, which contain lipid peroxides and their degradation products (Parthasarathy et al., 2010), but not when treated with LDL (Figure 3B), even though astrocytes internalize LDL (Figure S3A). On the other hand, neither LDL nor oxLDL induce LD formation in neurons (Figure S3B). These data suggested that astrocytes likely play an important role in internalizing and managing damaged lipid products from circulating lipoprotein particles in the brain.

We next asked what role neurons may play in generating lipoprotein particles. Neurons express ApoE in culture (Figures 3C and S3C) and following excitotoxicity *in vivo* (Xu et al., 2006). We reasoned that ApoE secreted by neurons (Figure S2I) could associate with lipoprotein particles and be internalized by astrocytes. We found that neuron-derived ApoE-GFP is transferred to astrocytes (Figures 3D and 3E), confirming both that neurons secrete ApoE and that the secreted ApoE can be taken up by astrocytes. Neurons are thought to release non-lipidated ApoE that associates with astrocyte-derived lipoprotein particles (DeMattos et al., 1998). However, we observed endogenous ApoE in cultured neurons co-localizing with BODIPY 493/503 (BD493), a neutral lipid stain, in small puncta and on Golgi-like structures (Figure 3C). Furthermore, ApoE was found largely in the pellet following high-speed centrifugation of neuron-conditioned media (Figure S2I) consistent with it being secreted as part of a lipid particle. To assess whether ApoE expressed in neurons facilitates the transfer of lipids to astrocytes, we performed FA transfer assays using cells cultured from wild-type and ApoE knockout mouse lines (Piedrahita et al., 1992). Knockout of ApoE in either neurons or astrocytes reduced transfer of Red-C12 to astrocytes (Figures 3F and S3D) supporting both ApoE-positive lipid release from neurons and a potential concurrent mechanism of transfer whereby neurons load FAs onto circulating lipoprotein particles secreted by astrocytes.

We then purified potential lipid particles from neuron-conditioned media using high-speed centrifugation and observed several types of particles ranging in size from 5 to 100 nm by transmission electron microscopy (Figure S3E). Extracellular vesicles are typically 30–100 nm in diameter suggesting that the smaller structures (5–30 nm) are likely lipid particles (van Niel et al., 2018). These data are consistent with lipid particles secreted from neuronal cell lines (Nelson and Sen, 2018) and support the conclusion that neurons release lipoprotein-like particles. To better assess whether neurons can make lipid particles, we employed focused ion beam scanning electron microscopy (FIB-SEM) technology (Xu et al., 2017), on adult mouse hippocampal tissue prepared with imidazole-buffered osmium tetroxide to stain lipids such as LDs and lipoprotein particles (Zhang et al., 2011; Rong et al., 2015). We observed membrane-bound lipid-dense structures in neurons (identified by the presence of synapses) in the pyramidal cell layer (Figures 3G–3J; Video S1). These structures were distinguishable from autophagosomes by their absence of organellar components (Figure S3F) and resembled lipoprotein particles (Rong et al., 2015). Similar lipid-dense, particle-like structures were seen in the ER (Figures 3I, 3J, and S3G), where lipid particles are synthesized. These lipid particles likely contribute to a fraction of the particles that stained positive for neutral lipids following NMDA treatment of cultured neurons (Figures 1E–1I).

Collectively, these results support the idea that neurons can synthesize lipid-rich particles in the ER and secrete them, opening the way for astrocytes to take them up by endocytosis. Assuming neuronal-derived FAs can attach to these lipid-rich particles, either in the ER or after the particles are secreted (through FA transporters), the result would be an extracellular pool of FA-loaded lipid particles available for uptake by astrocytes.

LD Formation in Astrocytes following Acute Stroke

Our results showing the transfer of FAs from neurons to astrocytes *in vitro* led us to ask whether this occurs *in vivo*, especially under conditions of oxidative stress. To address this, we performed a pial strip lesion in the rat brain cortex, a model system of acute stroke (Farr and Whishaw, 2002). The assay entails devascularizing a region of the motor cortex by removal of the pia mater. We first tested the efficacy of the assay by immunolabeling with markers of oxidative injury. A major source of tissue damage following stroke is excitotoxity caused by excess glutamate release (Lai et al., 2014). Consistent with this, we observed enhanced expression of the immediate early gene product c-fos, a marker of neuronal activation, in the stroke region compared to the contralateral hemisphere (Figures 4A and 4B). Following brain injury, astrocytes upregulate expression of the intermediate filament protein GFAP and microglia migrate to the region of damage (Ren et al., 2013; Ben Haim et al., 2015). We found an accumulation of GFAP-positive astrocytes and Iba1-positive microglia in the lesion site compared to the contralateral hemisphere (Figure S4A). Together these data confirm that our acute stroke model was sufficient to evoke oxidative injury.

We next examined whether acute stroke induced LD formation. As predicted, we observed LD accumulation in the lesion site but not in the contralateral hemisphere (Figures 4C and 4D). We were unable to detect LDs in neurons following stroke (Figure 4G), consistent with our *in vitro* assays showing that neurons transfer FAs to astrocytes (Figures 2 and 3). Instead, we found LD accumulation within the soma and along the processes of neighboring GFAP-positive astrocytes and Iba1-positive microglia (Figures 4H and S4B).

To test whether lipid particle-mediated FA transfer was involved in the accumulation of astrocytic LDs, we immunolabeled the tissue for ApoE. An increase in ApoE staining was observed in the lesion site as compared to the contralateral hemisphere (Figures 4E and 4F). In fact, a portion of neurons were found to express ApoE following acute stroke *in vivo* (Figure 4I). Together, these data support the role of lipid particle-mediated transfer of FAs from neurons to astrocytes following oxidative injury in the form of acute stroke.

Neural Activity Stimulates FA Transport from Neurons to Astrocytes

Since stroke involves oxidative damage to both neurons and astrocytes (Lai et al., 2014), we next sought to test whether hyperactivity in the neurons alone was sufficient to trigger FA transfer and LD formation in astrocytes *in vivo*. To this end, we used adeno-associated virus to express the chemogenetic receptor hM3Dq-mCh in neurons in the motor cortex of mice (Figures 5A and 5B). Intraperitoneal injection of the inert ligand clozapine-N-oxide (CNO) activates neurons expressing the hM3Dq receptor (Alexander et al., 2009). We stimulated neurons over 3 days and confirmed elevated neuronal activity by observing an upregulation of c-fos in neurons expressing hM3Dq treated with CNO, but not in those treated with saline, or CNO-treated neurons not expressing hM3Dq in the contralateral hemisphere (Figures 5C and 5D). We also observed an accumulation of LDs in the injected region after treatment with CNO (Figures 5E and 5F). Similar to the stroke model, we found LD accumulation
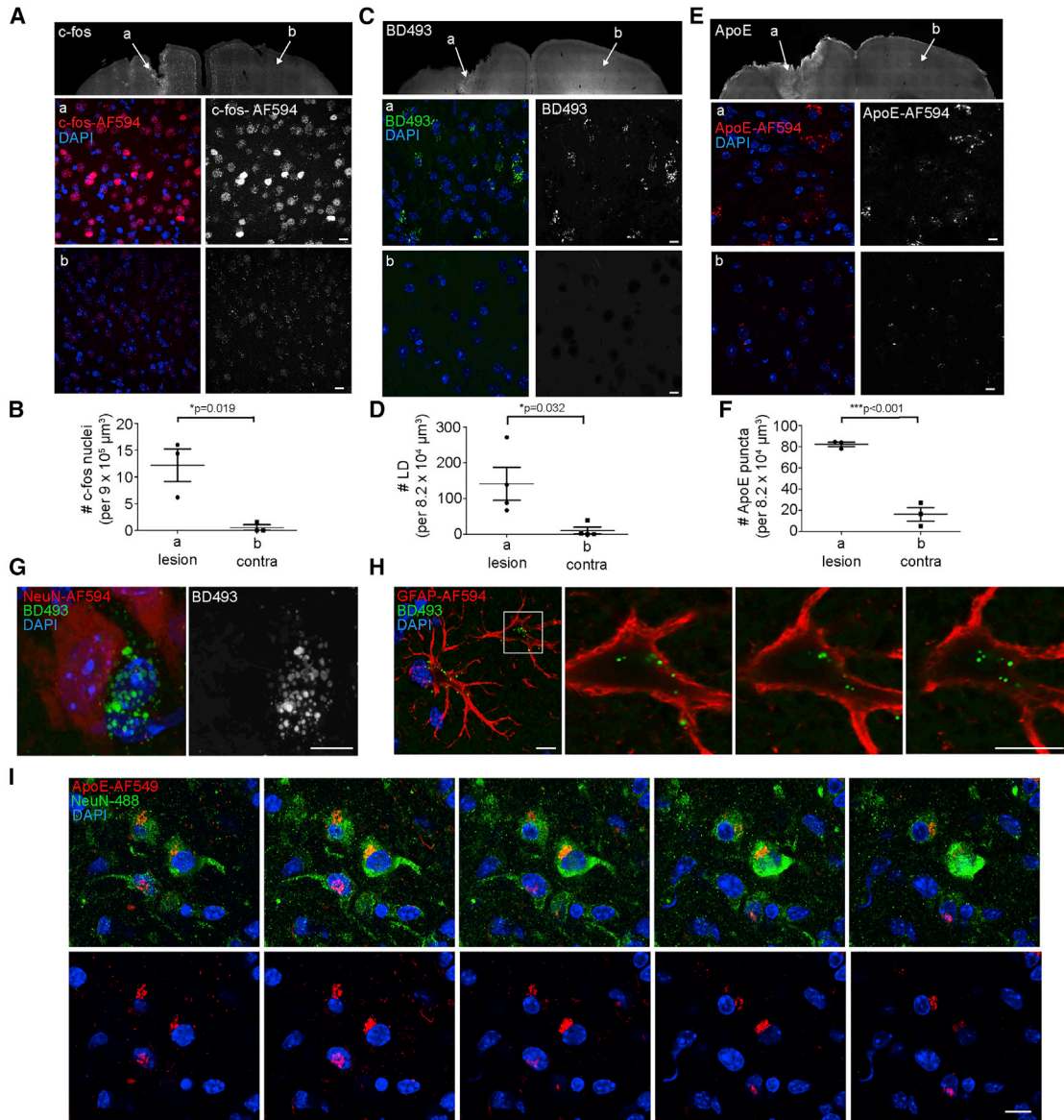
Figure 4. Astrocytes Accumulate LDs following Acute Stroke

(A–F) Cortex post-pial strip lesion stained with BD493 and immunostained for c-fos, or ApoE. Top panels: Tiled widefield images stitched with 10% overlap. Bottom panels are magnified maximum intensity projections of confocal images in the (a) lesioned hemisphere and (b) contralateral hemisphere. Scale bars are 10 μm. n = 4 animals for BD493 and n = 3 animals for c-fos and ApoE; mean ± SEM.

(G and H) Cortex post-pial strip lesion was immunostained with anti-NeuN or GFAP. Cropped maximum intensity projections of confocal images are displayed. Boxed area is shown as magnified confocal 0.5 μm sections in right panels. Scale bars are 10 μm.

(I) Cortex post-pial strip lesion was immunostained with anti-NeuN and ApoE. Cropped confocal 0.5 μm sections are displayed. Scale bars are 10 μm.

See Figure S4.

in astrocytes but not in neurons (Figures 5G and 5H). These results strongly suggest that neurons transfer FAs to astrocytic LDs in response to enhanced neural activity *in vivo*.

We next tested whether neuronal activity enhanced FA transfer *in vitro*. First, we expressed hM3Dq-mCh in cultured neurons and showed they could be activated in response to CNO as evidenced by increased c-fos staining (Figure 5I). We then performed a transfer assay using neurons expressing hM3Dq. We

observed enhanced FA transfer upon neuronal stimulation by CNO (Figures 5J and 5K). Red-C12 transfer, as opposed to hMD3q-mCh transfer, was confirmed by co-localization with BD493-positive LDs (Figure 5J). The increased transfer occurred without changes in neuronal apoptosis as assessed by DAPI nuclear staining (Figures S5A and S5B). Together, these results reveal that the transfer of FAs from neurons to astrocytes was significantly increased during periods of enhanced activity.
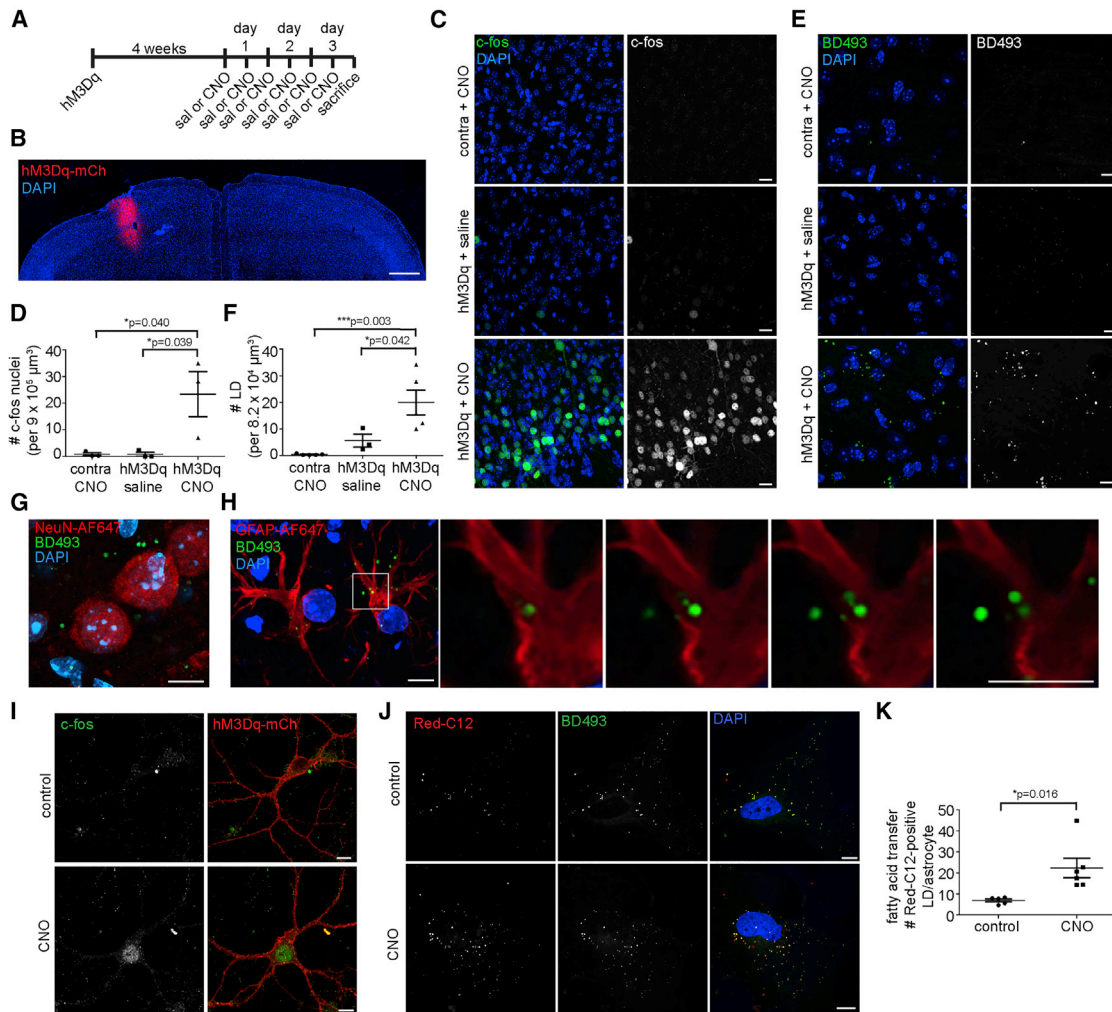
Figure 5. Neuronal Activity Stimulates FA Transfer to Astrocytes

(A) Schematic of *in vivo* activation assay. CNO, clozapine-N-oxide; Sal, and saline.

(B) Cortex expressing hM3Dq-mCh. Tiled confocal images were stitched with 10% overlap. Scale bars, 500 μm.

(C and D) Cortex following activation was immunostained for c-fos. Maximum intensity projections of confocal images are displayed. Scale bars, 20 μm. n = 3 animals/treatment; mean ± SEM.

(E and F) Cortex following activation was stained with BD493. Maximum intensity projections of confocal images are displayed. Scale bars, 10 μm. n = 3 animals/ treatment; mean ± SEM.

(G and H) Cortex in hM3Dq-mCh-expressing region following CNO treatment immunostained with anti-NeuN and anti-GFAP. Maximum intensity projections of confocal images are displayed. Boxed area is shown as magnified confocal 0.5 μm sections in right panels. Scale bars, 10 μm.

(I) Cropped confocal image of cultured neuron expressing hM3Gq-mCh treated with CNO for 90 min, fixed, and immunostained for c-fos. Scale bars, 10 μm.

(J and K) Cropped confocal images of astrocytes following FA transfer assay using neurons expressing hM3Dq-mCh ± CNO. 3 independent experiments; minimum of n = 5 coverslips/treatment; 27.1 ± 4.4 cells/coverslip; mean ± SEM.

See Figure S5.

Neuronal Activity Decreases LD Number in Astrocytes through Increased Lipolysis

Since neurons release FAs during periods of enhanced activity, and astrocytes sense neuronal activity through glutamate receptors such as the NMDA receptor (Anderson and Swanson, 2000; Dzamba et al., 2013), we wondered whether neuronal activity influences LD number in astrocytes. To assess this, we tested whether glutamate treatment alters the number of LDs in cultured astrocytes. A reduction in the number of LDs in cultured astrocytes treated with glutamate was observed (Figure S6A). This response involved the NMDA receptor since a similar reduction in the number of LDs occurred in astrocytes treated with NMDA, and the effect could be eliminated with the addition of the NMDA receptor antagonist AP5 (Figures 6A and 6B).

We speculated that the reduction in LD number in activated astrocytes was due to an increase in the rate of LD degradation. Astrocytes could utilize two possible mechanisms to break down LDs under NMDA receptor activation: lipophagy (the autophagic
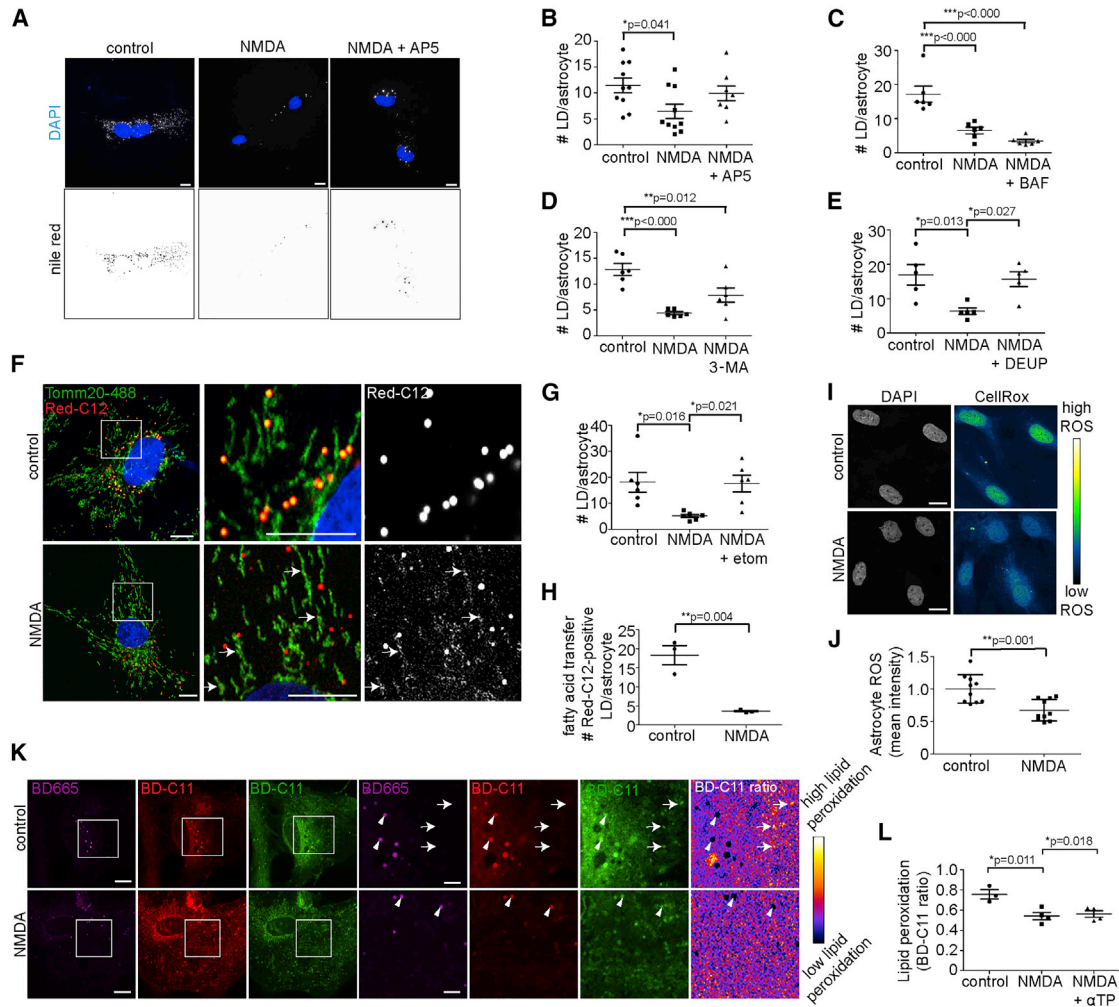
Figure 6. Astrocytes Consume FA in Response to Neuronal Activity

(A and B) Astrocytes ± NMDA and AP5 were fixed and stained with Nile Red, and the number of LDs was quantified. Top panel: Cropped widefield images of LDs displayed as maximum intensity projection on top of single DAPI image. Bottom panel: Inverted maximum intensity projection of LDs. 5 independent experiments; n = 8 coverslips/treatment; 21.2 ± 4.5 cells/coverslip; mean ± SEM.

(C) Astrocytes ± NMDA and BAF were fixed and stained with BD493, and the number of LDs was quantified. 3 independent experiments; n = 6 coverslips/treatment; 26.0 ± 5.3 cells/coverslip; mean ± SEM.

(D) Astrocytes ± NMDA and 3-MA were fixed and stained with BD493, and the number of LDs was quantified. 3 independent experiments; n = 6 coverslips/treatment; 28.1 ± 7.2 cells/coverslip; mean ± SEM.

(E) Astrocytes ± NMDA and DEUP were fixed and stained with BD493, and the number of LDs was quantified. 3 independent experiments; n = 5 coverslips/treatment; 24.3 ± 6.5 cells/coverslip; mean ± SEM.

(F) Cropped confocal image of astrocytes loaded with Red-C12 were chased ± NMDA and immunostained for TOMM20. Boxed area magnified on right. Scale bars,10 μm.

(G) Astrocytes ± NMDA and Etomoxir were fixed and stained with BD493, and the number of LDs was quantified. 3 independent experiments; n = 6 coverslips/treatment; 28.5 ± 4.1 cells/coverslip; mean ± SEM.

(H) Quantification of Red-C12-positive LDs in astrocytes following transfer assay ± NMDA. 3 independent experiments; n = 7 coverslips/treatment; 27.7 ± 4.8 cells/coverslip; mean ± SEM.

(I and J) Cropped confocal image of astrocytes ± NMDA were labeled with CellRox. Mean intensity of nuclei was quantified. 4 independent experiments; n = 7 coverslips/treatment; 29.5 ± 5.2 cells/coverslip; mean ± SEM.

(K and L) Cropped confocal image of astrocytes ± NMDA labeled with BD665 and BD-C11. Total and peroxidated lipid in red and green, respectively. Boxed area highlighted on right. Arrows, peroxidated puncta. Arrowheads, low lipid peroxidation in LDs. Scale bars, 10 μm. α-tocopherol (αTP). 2 independent experiments; minimum of n = 3 coverslips/treatment; 24.5 ± 3.5 cells/coverslip; mean ± SEM. See Figure S6.

degradation of LDs) or lipolysis by cytoplasmic lipases. We found that autophagy inhibitors 3-MA and bafilomycin had no effect on NMDA-dependent LD degradation (Figures 6C and 6D).

By contrast, the pan-lipase inhibitor DEUP prevented NMDA-dependent LD degradation (Figure 6E). These data indicate that cytoplasmic lipases rather than autophagic mechanisms

were responsible for breaking down astrocytic LDs under increased neuronal activity.

Astrocytes Degrade FAs and Neutralize ROS in Response to Neural Activity

We next asked whether FAs liberated from LDs are consumed by FA oxidation in mitochondria. For this purpose, we preloaded astrocytes with Red-C12 and tracked the labeled FA after NMDA treatment to see whether it was delivered to mitochondria. Consistent with this, Red-C12 appeared in mitochondria as early as 4 h after NMDA treatment (Figure 6F). Co-treatment of astrocytes with NMDA and etomoxir, a carnitine palmitoyltransferase-1 inhibitor that prevents FA transport into mitochondria, decreased the NMDA-dependent reduction in the number of LDs (Figure 6G), suggesting astrocytes deliver FAs to mitochondria for β-oxidation in response to neuronal activity. We also observed a reduction in Red-C12 (originating from neurons) in astrocytes in our transfer assay when NMDA was added (Figure 6H), which would occur if astrocytes degrade neuron-derived FAs in response to neuronal activity. These results support a model in which neurons augment FA transport to astrocytes in response to neuronal activity (Figure 5), while astrocytes degrade the incoming FAs in response to that same activity.

Because mitochondrial β-oxidation itself can produce ROS (Schönfeld and Reiser, 2017), we reasoned that astrocytes with increased mitochondrial β-oxidation under conditions of excess neuronal activity must have a mechanism to neutralize ROS; otherwise, they would jeopardize their own health. To examine this, we measured oxidative stress levels by staining astrocytes with the CellRox probe that fluoresces green upon oxidation by ROS in the nucleus. A decrease in CellRox fluorescence was observed in cultured astrocytes treated with NMDA, indicating decreased oxidative stress levels in these cells (Figures 6I, 6J, and S6B). As a second test, we measured lipid peroxidation in astrocytes using the BD-C11 ratiometric lipid peroxidation sensor. There was a decrease in levels of peroxidated lipids in both LDs and the surrounding membranes upon treatment of astrocytes with NMDA, indicating lipid peroxidation in astrocytes was reduced (Figures 6K and 6L). No further reduction in lipid peroxidation was observed when astrocytes were treated with NMDA plus α-tocopherol (Figure 6L). Taken together, these results suggest that, under excess neuronal activity, astrocytes consume incoming neuronal-derived FAs in mitochondria through β-oxidation, and this is associated with decreased ROS and lipid peroxidation levels in astrocytes.

Astrocytes Are Equipped with the Machinery to Neutralize ROS

Since astrocytes internalize peroxidated lipids from neurons, we reasoned that astrocytes must be equipped with the molecular machinery to neutralize the oxidative stress and metabolize the lipids. One way this might occur is if astrocytes upregulate genes responsible for oxidative stress management in response to LD accumulation. To test this, we profiled the transcriptome of cultured astrocytes, in which the cells were analyzed based on whether they contained LDs. Astrocytes were stained with Nile Red to selectively label LDs under 488 nm excitation (Greenspan et al., 1985). Cells containing LDs were then separated from

those that did not by fluorescence activated cell sorting. RNA sequencing (RNA-seq) analysis was performed on both of the isolated cell populations (Figures S7A and S7B). By comparing the gene expression profile of our cultured astrocytes to an existing RNA-seq database of cell types in the brain (Zhang et al., 2014), we confirmed the purity of our astrocyte cultures, ruling out the possibility that contaminating cell types represented the cells that had LD buildup (Figure S7C). Notably, a group of genes related to neutralizing oxidative stress and lipid metabolism were upregulated in astrocytes containing LDs (Figures 7A, 7B, and S7C).

Our differential gene expression analysis also revealed that astrocytes expressed higher levels of oxidative stress- and lipid metabolism-related genes compared to neurons, regardless of whether they were purified from the brain or cultured, or if they contained LDs (Figures 7B and 7C). Among the genes enriched in astrocytes containing LDs were those responsible for protection from free-FA toxicity (*Gpx8*), neutralizing oxidative species superoxide radicals (*Sod1* and *Sod3*) and hydrogen peroxide (*Cat*) and genes involved in FA transport (*Fabp5* and *Fabp7*) and FA metabolism (*Acsbg1* and *Dbi*). Interestingly, RNA-seq analysis of cells purified from the brain shows that, while microglia and oligodendrocytes also express genes involved in responding to oxidative stress, they used distinct sets of genes from astrocytes and each other. Therefore, each glial cell type would appear to use a unique machinery to manage oxidative stress at basal levels. However, astrocytes upregulate these genes in response to LD accumulation (Figure 7B). Importantly, neurons express comparatively low levels of these genes, indicating they are not adequately equipped to handle oxidative stress and lipid accumulation (Figures 7B and 7C). This supports the reliance of neurons on neighboring glia, such as astrocytes, to metabolize excess FAs and neutralize oxidative stress.

DISCUSSION

The regulation of lipid metabolism is critical for avoiding FA toxicity during neuronal activity and ultimately for maintaining the health of the brain. Here, we discovered that avoidance of FA toxicity in neurons is achieved by the activity-dependent coordination between neurons and astrocytes in the metabolism of FAs. Specifically, hyperactive neurons release toxic lipids in ApoE-positive lipid particles that neighboring astrocytes take up by endocytosis. These transferred FAs are used as metabolic intermediates for increased mitochondrial oxidation and detoxification in the astrocyte in response to neural activity. As discussed below, we propose that this mechanism allows astrocytes to protect hyperactive neurons from FA toxicity.

The accumulation of lipids in hyperactive neurons is toxic not only because of the susceptibility of these lipids to peroxidation. Overabundance of FAs may enter nonoxidative metabolic pathways triggering excessive ceramide production that is toxic to cells (Unger et al., 2010). Recent work has also shown that, in LD-defective cells, FAs can be converted into acylcarnitines, which cause mitochondrial fragmentation and dysfunction and ROS production (Nguyen et al., 2017). This process is likely to have profound consequences in hyperactive neurons since dysfunctional mitochondria are unable to metabolize FAs and
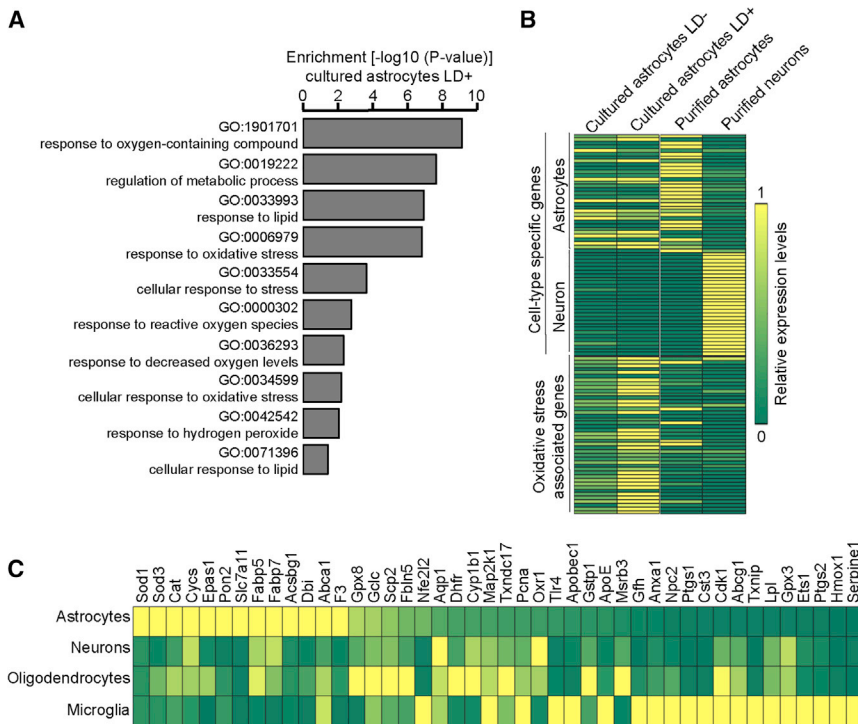
Figure 7. Astrocytes Containing LDs Upregulate Genes Associated with Oxidant Detoxification

(A) Gene ontology (GO) pathways enriched in cultured astrocytes containing LDs. See Table S1.

(B) Astrocytes enriched for genes associated with oxidative stress. Relative gene expression levels in different cell types were presented in the heatmap.

(C) Expression levels of selected genes associated with oxidative stress and enriched in astrocytes containing LDs in (B). The color bar is the same as in (B).

See Figure S7.

their ROS production causes peroxidation of lipids on membranes. This is further accentuated by FA release from peroxidated membranes undergoing autophagy, generating a runaway system of toxic FA buildup. To relieve this stress, the neuron would need a mechanism to expel its excess FAs, whether they are peroxidated or not.

The species of lipids being peroxidated and transferred remains to be determined. The BODIPY-conjugated FAs used in our study are incorporated into membranes presumably as phospholipids. These membranes can be degraded by autophagy, converted back to FAs, and stored in LDs or lipoprotein particles as neutral lipids. As phospholipids are well-known targets of lipid peroxidation (Ayala et al., 2014), perhaps lipid particles released from healthy neurons contain small amounts of peroxidated phospholipids, while hyperactive neurons release particles with more extensive peroxidation including neutral lipids. The degree of saturation of the transferred lipids is also unknown.

We envision two non-exclusive pathways for release of lipids from hyperactive neurons. The first involves direct transport of free FAs through ATP-binding cassette (ABC) transporters on the neuronal cell surface. Prior work has shown that such transfer can lead to loading of circulating lipoprotein particles outside the cell (Kim et al., 2007). A reduction in FA transfer (Figure 3) and LD formation (Liu et al., 2017) following ApoE knockout in glia supports this mechanism of transfer. A second pathway for lipid release is by loading FAs, as neutral lipids and/or phospholipids, into lipid particles within the lumen of the ER in the neuron. The ER-localized lipid particles are then packaged into membrane-bound secretory vesicles that target to the plasma membrane for release. Supporting this exit possibility, we found reduced

FA transfer from ApoE knockout neurons and observed lipid particles in the ER and secretory vesicles in neurons by electron microscopy. The identity of the lipid particles released by neurons remains unknown. Further work is needed to characterize these particles and clarify the relative extent to which hyperactive neurons use the lipid particle release pathway, the ABC transporter-based pathway, or both in expelling excess FAs.

Our study supports a role for ApoE, a lipid transport protein associated with lipoprotein particles, in FA transfer from neurons to glia (Liu et al., 2017). We found that ApoE expression is upregulated in neurons in response to oxidative stress in order to increase their FA efflux. Further evidence for the role of ApoE in FA efflux from neurons is the toxic effect of the *ApoE4* polymorphism, with reduced lipid binding and secretion capacity, when it is expressed in neurons (Buttini et al., 2010; Mahley, 2016). This could be explained if neurons expressing the *ApoE4* allele do not release FAs as efficiently as wild-type ApoE, and as a result undergo greater lipotoxicity and/or damage by lipid peroxidation. Introducing the *ApoE4* allele into astrocytes has no similar effect on brain toxicity (Buttini et al., 2010; Mahley, 2016). Significantly, ApoE4 is the leading risk factor for late-onset Alzheimer's disease and determines neuronal susceptibility to excitotoxicity (Aoki et al., 2003; Buttini et al., 2010). Apolipoproteins such as ApoE, therefore, may play a key role in supporting neuronal health by channeling FAs away from neurons to astrocytes.

Astrocytes endocytose ApoE-positive lipid particles and sequester FAs into LDs. Yet the fate of the FAs does not end in the LD; FAs can be consumed by oxidative phosphorylation in mitochondria. We found that when astrocytes are stimulated with NMDA, they consume their LDs via mitochondrial oxidative metabolism and yet they have reduced levels of ROS. We suspect that a converging pathway may be activated to counteract the ROS generated by increased β-oxidation and mitochondrial activity. Activation of antioxidant enzymes by post-translational modifications would certainly fit the timescale of the effects that we observe.

Why might the effect of NMDA on astrocytes be significant for understanding neuronal transmission? Astrocytes express NMDA receptors, which allow them to respond to neuronal

activity (Dzamba et al., 2013). Through NMDA receptors, glutamate released by active neurons would trigger FA consumption and ATP production by astrocytes. Interestingly, glutamate also triggers ATP release by astrocytes (Zhang et al., 2003), and ATP released by astrocytes activates interneurons, resulting in increased synaptic inhibition (Bowser and Khakh, 2004). Thus, astrocytes may convert neuron-derived FAs into ATP in order to increase the activity of inhibitory interneurons. Increased interneuron activity would provide elevated inhibitory transmission onto the hyperactive neurons, potentially relieving them of excitotoxicity. Such a feedback loop from astrocytes to neurons could be an important mechanism for attenuating the activity of hyperactive neurons and protect them from the damage associated with excess FA accumulation.

STAR★METHODS

Detailed methods are provided in the online version of this paper and include the following:

- KEY RESOURCES TABLE
- CONTACT FOR REAGENT AND RESOURCE SHARING
- EXPERIMENTAL MODEL AND SUBJECT DETAILS
  - Animals
- METHOD DETAILS
  - Primary culture of hippocampal neurons and astrocytes
  - Cloning ApoE-GFP
  - Confocal and widefield imaging
  - Mitochondria fragmentation and surface area assay
  - Autophagy induction assay
  - Lipid droplet assay
  - Fatty acid and ApoE transfer assays
  - Fatty acid pulse-chase assays
  - Lipoprotein particle depletion assay
  - Lipid peroxidation and ROS assays
  - Electron microscopy of purified particles
  - Mouse brain sample preparation for FIB-SEM
  - FIB-SEM imaging of mouse brain sample
  - Cell Sorting and RNA-seq library preparation
  - Gene expression level testing and gene ontology analysis
  - Pial strip devascularization and chemogenetic stimulations
  - Histology
- QUANTIFICATION AND STATISTICAL ANALYSIS
- DATA AND SOFTWARE AVAILABILITY

REFERENCES

Alexander, G.M., Rogan, S.C., Abbas, A.I., Armbruster, B.N., Pei, Y., Allen, J.A., Nonneman, R.J., Hartmann, J., Moy, S.S., Nicolelis, M.A., et al. (2009). Remote control of neuronal activity in transgenic mice expressing evolved G protein-coupled receptors. Neuron 63, 27–39.

Anderson, C.M., and Swanson, R.A. (2000). Astrocyte glutamate transport: review of properties, regulation, and physiological functions. Glia 32, 1–14.

Aoki, K., Uchihara, T., Sanjo, N., Nakamura, A., Ikeda, K., Tsuchiya, K., and Wakayama, Y. (2003). Increased expression of neuronal apolipoprotein E in human brain with cerebral infarction. Stroke 34, 875–880.

Ayala, A., Muñoz, M.F., and Argüelles, S. (2014). Lipid peroxidation: production, metabolism, and signaling mechanisms of malondialdehyde and 4-hydroxy-2-nonenal. Oxid. Med. Cell. Longev. 2014, 360438.

Bailey, A.P., Koster, G., Guillermier, C., Hirst, E.M., MacRae, J.I., Lechene, C.P., Postle, A.D., and Gould, A.P. (2015). Antioxidant Role for Lipid Droplets in a Stem Cell Niche of Drosophila. Cell 163, 340–353.

Beaudoin, G.M., 3rd, Lee, S.H., Singh, D., Yuan, Y., Ng, Y.G., Reichardt, L.F., and Arikkath, J. (2012). Culturing pyramidal neurons from the early postnatal mouse hippocampus and cortex. Nat. Protoc. 7, 1741–1754.

Bélanger, M., and Magistretti, P.J. (2009). The role of astroglia in neuroprotection. Dialogues Clin. Neurosci. 11, 281–295.

Bélanger, M., Allaman, I., and Magistretti, P.J. (2011). Brain energy metabolism: focus on astrocyte-neuron metabolic cooperation. Cell Metab. 14, 724–738.

Ben Haim, L., Carrillo-de Sauvage, M.A., Ceyzériat, K., and Escartin, C. (2015). Elusive roles for reactive astrocytes in neurodegenerative diseases. Front. Cell. Neurosci. 9, 278.

Bolte, S., and Cordelières, F.P. (2006). A guided tour into subcellular colocalization analysis in light microscopy. J. Microsc. 224, 213–232.

Bowser, D.N., and Khakh, B.S. (2004). ATP excites interneurons and astrocytes to increase synaptic inhibition in neuronal networks. J. Neurosci. 24, 8606–8620.

Buttini, M., Masliah, E., Yu, G.Q., Palop, J.J., Chang, S., Bernardo, A., Lin, C., Wyss-Coray, T., Huang, Y., and Mucke, L. (2010). Cellular source of apolipoprotein E4 determines neuronal susceptibility to excitotoxic injury in transgenic mice. Am. J. Pathol. 177, 563–569.

Cembrowski, M.S., Wang, L., Sugino, K., Shields, B.C., and Spruston, N. (2016). Hipposeq: a comprehensive RNA-seq database of gene expression in hippocampal principal neurons. eLife 5, e14997.

DeMattos, R.B., Curtiss, L.K., and Williams, D.L. (1998). A minimally lipidated form of cell-derived apolipoprotein E exhibits isoform-specific stimulation of neurite outgrowth in the absence of exogenous lipids or lipoproteins. J. Biol. Chem. 273, 4206–4212.

Dzamba, D., Honsa, P., and Anderova, M. (2013). NMDA Receptors in Glial Cells: Pending Questions. Curr. Neuropharmacol. 11, 250–262.

Farr, T.D., and Whishaw, I.Q. (2002). Quantitative and qualitative impairments in skilled reaching in the mouse (Mus musculus) after a focal motor cortex stroke. Stroke 33, 1869–1875.

Greenspan, P., Mayer, E.P., and Fowler, S.D. (1985). Nile red: a selective fluorescent stain for intracellular lipid droplets. J. Cell Biol. 100, 965–973.

Haba, K., Ogawa, N., Mizukawa, K., and Mori, A. (1991). Time course of changes in lipid peroxidation, pre- and postsynaptic cholinergic indices, NMDA receptor binding and neuronal death in the gerbil hippocampus following transient ischemia. Brain Res. 540, 116–122.

Huang, D.W., Sherman, B.T., Tan, Q., Collins, J.R., Alvord, W.G., Roayaei, J., Stephens, R., Baseler, M.W., Lane, H.C., and Lempicki, R.A. (2007a). The DAVID Gene Functional Classification Tool: a novel biological module-centric algorithm to functionally analyze large gene lists. Genome Biol. 8, R183.

Huang, D.W., Sherman, B.T., Tan, Q., Kir, J., Liu, D., Bryant, D., Guo, Y., Stephens, R., Baseler, M.W., Lane, H.C., and Lempicki, R.A. (2007b). DAVID Bioinformatics Resources: expanded annotation database and novel algorithms to better extract biology from large gene lists. Nucleic Acids Res. 35, W169–W175.

Kasthuri, N., Hayworth, K.J., Berger, D.R., Schalek, R.L., Conchello, J.A., Knowles-Barley, S., Lee, D., Vázquez-Reina, A., Kaynig, V., Jones, T.R., et al. (2015). Saturated Reconstruction of a Volume of Neocortex. Cell 162, 648–661.

Kim, W.S., Rahmanto, A.S., Kamili, A., Rye, K.A., Guillemin, G.J., Gelissen, I.C., Jessup, W., Hill, A.F., and Garner, B. (2007). Role of ABCG1 and ABCA1 in regulation of neuronal cholesterol efflux to apolipoprotein E discs and suppression of amyloid-beta peptide generation. J. Biol. Chem. 282, 2851–2861.

Klausner, R.D., Donaldson, J.G., and Lippincott-Schwartz, J. (1992). Brefeldin A: insights into the control of membrane traffic and organelle structure. J. Cell Biol. 116, 1071–1080.

Lai, T.W., Zhang, S., and Wang, Y.T. (2014). Excitotoxicity and stroke: identifying novel targets for neuroprotection. Prog. Neurobiol. 115, 157–188.

Langmead, B., and Salzberg, S.L. (2012). Fast gapped-read alignment with Bowtie 2. Nat. Methods 9, 357–359.

Li, B., and Dewey, C.N. (2011). RSEM: accurate transcript quantification from RNA-Seq data with or without a reference genome. BMC Bioinformatics 12, 323.

Lippincott-Schwartz, J., Yuan, L., Tipper, C., Amherdt, M., Orci, L., and Klausner, R.D. (1991). Brefeldin A's effects on endosomes, lysosomes, and the TGN suggest a general mechanism for regulating organelle structure and membrane traffic. Cell 67, 601–616.

Liu, L., Zhang, K., Sandoval, H., Yamamoto, S., Jaiswal, M., Sanz, E., Li, Z., Hui, J., Graham, B.H., Quintana, A., and Bellen, H.J. (2015). Glial lipid droplets and ROS induced by mitochondrial defects promote neurodegeneration. Cell 160, 177–190.

Liu, L., MacKenzie, K.R., Putluri, N., Maletić-Savatić, M., and Bellen, H.J. (2017). The Glia-Neuron Lactate Shuttle and Elevated ROS Promote Lipid Synthesis in Neurons and Lipid Droplet Accumulation in Glia via APOE/D. Cell Metab. 26, 719–737.e6.

Mahley, R.W. (2016). Central Nervous System Lipoproteins: ApoE and Regulation of Cholesterol Metabolism. Arterioscler. Thromb. Vasc. Biol. 36, 1305–1315.

Martin, M. (2011). Cutadapt Removes Adapter Sequences From High-Throughput Sequencing Reads. EMBnet J. 17, 10–12.

Nelson, T.J., and Sen, A. (2018). Apolipoprotein E particle size is increased in Alzheimer's disease. Alzheimers Dement. (Amst.) 11, 10–18.

Nguyen, D., Alavi, M.V., Kim, K.Y., Kang, T., Scott, R.T., Noh, Y.H., Lindsey, J.D., Wissinger, B., Ellisman, M.H., Weinreb, R.N., et al. (2011). A new vicious cycle involving glutamate excitotoxicity, oxidative stress and mitochondrial dynamics. Cell Death Dis. 2, e240.

Nguyen, T.B., Louie, S.M., Daniele, J.R., Tran, Q., Dillin, A., Zoncu, R., Nomura, D.K., and Olzmann, J.A. (2017). DGAT1-Dependent Lipid Droplet Biogenesis Protects Mitochondrial Function during Starvation-Induced Autophagy. Dev. Cell 42, 9–21.e5.

Parihar, M.S., and Hemnani, T. (2004). Experimental excitotoxicity provokes oxidative damage in mice brain and attenuation by extract of Asparagus racemosus. J. Neural Transm. (Vienna) 111, 1–12.

Parthasarathy, S., Raghavamenon, A., Garelnabi, M.O., and Santanam, N. (2010). Oxidized low-density lipoprotein. Methods Mol. Biol. 610, 403–417.

Piedrahita, J.A., Zhang, S.H., Hagaman, J.R., Oliver, P.M., and Maeda, N. (1992). Generation of mice carrying a mutant apolipoprotein E gene inactivated by gene targeting in embryonic stem cells. Proc. Natl. Acad. Sci. USA 89, 4471–4475.

Pitas, R.E., Boyles, J.K., Lee, S.H., Hui, D., and Weisgraber, K.H. (1987). Lipoproteins and their receptors in the central nervous system. Characterization of the lipoproteins in cerebrospinal fluid and identification of apolipoprotein B,E(LDL) receptors in the brain. J. Biol. Chem. 262, 14352–14360.

Rambold, A.S., Cohen, S., and Lippincott-Schwartz, J. (2015). Fatty acid trafficking in starved cells: regulation by lipid droplet lipolysis, autophagy, and mitochondrial fusion dynamics. Dev. Cell 32, 678–692.

Redmann, M., Benavides, G.A., Berryhill, T.F., Wani, W.Y., Ouyang, X., Johnson, M.S., Ravi, S., Barnes, S., Darley-Usmar, V.M., and Zhang, J. (2017). Inhibition of autophagy with bafilomycin and chloroquine decreases mitochondrial quality and bioenergetic function in primary neurons. Redox Biol. 11, 73–81.

Ren, Z., Iliff, J.J., Yang, L., Yang, J., Chen, X., Chen, M.J., Giese, R.N., Wang, B., Shi, X., and Nedergaard, M. (2013). 'Hit & Run' model of closed-skull traumatic brain injury (TBI) reveals complex patterns of post-traumatic AQP4 dysregulation. J. Cereb. Blood Flow Metab. 33, 834–845.

Reynolds, I.J., and Hastings, T.G. (1995). Glutamate induces the production of reactive oxygen species in cultured forebrain neurons following NMDA receptor activation. J. Neurosci. 15, 3318–3327.

Rong, X., Wang, B., Dunham, M.M., Hedde, P.N., Wong, J.S., Gratton, E., Young, S.G., Ford, D.A., and Tontonoz, P. (2015). Lpcat3-dependent production of arachidonoyl phospholipids is a key determinant of triglyceride secretion. eLife. Published online March 25, 2015. https://doi.org/10.7554/eLife.06557.

Schönfeld, P., and Reiser, G. (2013). Why does brain metabolism not favor burning of fatty acids to provide energy? Reflections on disadvantages of the use of free fatty acids as fuel for brain. J. Cereb. Blood Flow Metab. 33, 1493–1499.

Schönfeld, P., and Reiser, G. (2017). Brain energy metabolism spurns fatty acids as fuel due to their inherent mitotoxicity and potential capacity to unleash neurodegeneration. Neurochem. Int. 109, 68–77.

Seiler, A., Schneider, M., Förster, H., Roth, S., Wirth, E.K., Culmsee, C., Plesnila, N., Kremmer, E., Rådmark, O., Wurst, W., Bornkamm, G.W., Schweizer, U., and Conrad, M. (2008). Glutathione peroxidase 4 senses and translates oxidative stress into 12/15-lipoxygenase dependent- and AIF-mediated cell death. Cell Metab. 8, 237–248.

Sultana, R., Perluigi, M., and Butterfield, D.A. (2013). Lipid peroxidation triggers neurodegeneration: a redox proteomics view into the Alzheimer disease brain. Free Radic. Biol. Med. 62, 157–169.

Trajkovic, K., Hsu, C., Chiantia, S., Rajendran, L., Wenzel, D., Wieland, F., Schwille, P., Brügger, B., and Simons, M. (2008). Ceramide triggers budding of exosome vesicles into multivesicular endosomes. Science 319, 1244–1247.

Trapnell, C., Pachter, L., and Salzberg, S.L. (2009). TopHat: discovering splice junctions with RNA-Seq. Bioinformatics 25, 1105–1111.

Trapnell, C., Williams, B.A., Pertea, G., Mortazavi, A., Kwan, G., van Baren, M.J., Salzberg, S.L., Wold, B.J., and Pachter, L. (2010). Transcript assembly and quantification by RNA-Seq reveals unannotated transcripts and isoform switching during cell differentiation. Nat. Biotechnol. *28*, 511–515.

Trapnell, C., Roberts, A., Goff, L., Pertea, G., Kim, D., Kelley, D.R., Pimentel, H., Salzberg, S.L., Rinn, J.L., and Pachter, L. (2012). Differential gene and transcript expression analysis of RNA-seq experiments with TopHat and Cufflinks. Nat. Protoc. *7*, 562–578.

Unger, R.H., Clark, G.O., Scherer, P.E., and Orci, L. (2010). Lipid homeostasis, lipotoxicity and the metabolic syndrome. Biochim. Biophys. Acta *1801*, 209–214.

van Niel, G., D'Angelo, G., and Raposo, G. (2018). Shedding light on the cell biology of extracellular vesicles. Nat. Rev. Mol. Cell Biol. *19*, 213–228.

Wang, H., Wei, E., Quiroga, A.D., Sun, X., Touret, N., and Lehner, R. (2010). Altered lipid droplet dynamics in hepatocytes lacking triacylglycerol hydrolase expression. Mol. Biol. Cell *21*, 1991–2000.

Xu, Q., Bernardo, A., Walker, D., Kanegawa, T., Mahley, R.W., and Huang, Y. (2006). Profile and regulation of apolipoprotein E (ApoE) expression in the CNS in mice with targeting of green fluorescent protein gene to the ApoE locus. J. Neurosci. *26*, 4985–4994.

Xu, C.S., Hayworth, K.J., Lu, Z., Grob, P., Hassan, A.M., García-Cerdán, J.G., Niyogi, K.K., Nogales, E., Weinberg, R.J., and Hess, H.F. (2017). Enhanced FIB-SEM systems for large-volume 3D imaging. eLife. Published online May 13, 2017. https://doi.org/10.7554/eLife.25916.

Zhang, J.M., Wang, H.K., Ye, C.Q., Ge, W., Chen, Y., Jiang, Z.L., Wu, C.P., Poo, M.M., and Duan, S. (2003). ATP released by astrocytes mediates glutamatergic activity-dependent heterosynaptic suppression. Neuron *40*, 971–982.

Zhang, L., Song, J., Cavigiolio, G., Ishida, B.Y., Zhang, S., Kane, J.P., Weisgraber, K.H., Oda, M.N., Rye, K.A., Pownall, H.J., and Ren, G. (2011). Morphology and structure of lipoproteins revealed by an optimized negative-staining protocol of electron microscopy. J. Lipid Res. *52*, 175–184.

Zhang, Y., Chen, K., Sloan, S.A., Bennett, M.L., Scholze, A.R., O'Keeffe, S., Phatnani, H.P., Guarnieri, P., Caneda, C., Ruderisch, N., et al. (2014). An RNA-sequencing transcriptome and splicing database of glia, neurons, and vascular cells of the cerebral cortex. J. Neurosci. *34*, 11929–11947.

STAR★METHODS

KEY RESOURCES TABLE

REAGENT or RESOURCE	SOURCE	IDENTIFIER
Antibodies		
Rabbit polyclonal anti-NeuN	EMD Millipore	Cat# ABN78 RRID: AB_10807945
Mouse monoclonal anti-Tuj1	Biolegend	Cat# 801202 RRID:AB_10063408
Chicken polyclonal anti-GFAP	Abcam	Cat# ab4674 RRID: AB_304558
Rabbit polyclonal anti-Iba1	Wako Chemicals	Cat# 019-19741 RRID: AB_839504
Goat polyclonal anti-ApoE	Millipore-Sigma	Cat# 178479 RRID:AB_10682965
Rabbit polyclonal anti-LC3b	Abcam	Cat# ab48394 RRID:AB_881433
Rabbit polyclonal anti-TOMM20	Abcam	Cat# ab186735 RRID:AB_2716623
Rabbit monoclonal anti-c-fos	Cell Signaling Technology	Cat# 2250 RRID:AB_2247211
Donkey anti-rabbit IgG (H+L) Alexa Fluor 488	Thermo Fisher Scientific	Cat# A-21206 RRID:AB_2535792
Donkey anti-goat IgG (H+L) Alexa Fluor 488	Thermo Fisher Scientific	Cat# A-11055 RRID:AB_2534102
Goat anti-mouse IgG (H+L) Alexa Fluor 488	Thermo Fisher Scientific	Cat# A-11001 RRID:AB_2534069
Goat anti-chicken IgY (H+L) Alexa Fluor 488	Thermo Fisher Scientific	Cat# A-11039 RRID:AB_2534096
Bovine anti-goat IgG (H+L) DyLight 549	Jackson ImmunoReseach	805-505-180
Goat anti-rabbit IgG (H+L) Alexa Fluor 594	Thermo Fisher Scientific	Cat# A-11037 RRID:AB_2534095
Goat anti-chicken IgY (H+L) Alexa Fluor 594	Thermo Fisher Scientific	Cat# A-11042 RRID:AB_2534099
Goat anti-chicken IgY (H+L) Alexa Fluor 647	Thermo Fisher Scientific	Cat# A-21449 RRID:AB_2535866
Bacterial and Virus Strains		
AAV2-hCamKII-DIO-hM3Dq-2A-mCherry	Janelia Virus Services	N/A
AAV-SL1-hSyn-cre	Janelia Virus Services	N/A
AAV2-CAG-cre	Janelia Virus Services	N/A
AAV2.1-hSyn-DIO-hM3Dq-mCherry	UNC Vector Core	N/A
AAV2/1-CAG-ApoE-GFP-WPRE	Janelia Virus Services	N/A
Chemicals, Peptides, and Recombinant Proteins		
BODIPY 665/676 (BD665)	Thermo Fisher Scientific	Cat# B3932
BODIPY 493/503 (BD493)	Thermo Fisher Scientific	Cat# D3922
BODIPY 581/591 C11 (Lipid peroxidation sensor) (BD-C11)	Thermo Fisher Scientific	Cat# D3861
BODIPY −558/568 C12 (4,4-Difluoro-5-(2-Thienyl)-4-Bora-3a,4a-Diaza-s-Indacene-3-Dodecanoic Acid) (Red-C12)	Thermo Fisher Scientific	Cat# D3835
Nile Red	Thermo Fisher Scientific	Cat# N1142
Oleic acid-albumin	Millipore-Sigma	Cat# O3008
Linoleic acid-albumin	Millipore-Sigma	Cat# L9530
CellTracker Green CMFDA Dye	Thermo Fisher Scientific	Cat# C2925
Cytosine-beta-D-arabinofuranose hydrochloride (AraC)	Thermo Fisher Scientific	Cat# J6567103
Bafilomycin A1 (BAF)	Millipore-Sigma	Cat# B1793
Brefeldin A (BFA)	Abcam	Cat# ab120299
3-Methyladenine (3-MA)	Thermo Fisher Scientific	Cat# 18-949
Diethylumbelliferyl phosphate (DEUP)	Millipore-Sigma	Cat# D7692
Pitstop2	Millipore-Sigma	Cat# SML1169
GW4869	Millipore-Sigma	Cat# 567715
Etomoxir	Thermo Fisher Scientific	Cat# 50-945-50001

(Continued on next page)

Continued

REAGENT or RESOURCE	SOURCE	IDENTIFIER
CellRox Green Reagent	Thermo Fisher Scientific	Cat# C10444
NMDA	Tocris Bioscience	Cat# 0114
D-AP5	Tocris Bioscience	Cat# 0106
L-Glutamic Acid	Thermo Fisher Scientific	Cat# ICN19467780
α-tocopherol	Thermo Fisher Scientific	Cat# AC421031000
BODIPY 515/520- Low-Density Lipoprotein (LDL) from Human Plasma (BD-LDL)	Thermo Fisher Scientific	Cat# L3483
Low Density Lipoprotein from Human Plasma (LDL)	Thermo Fisher Scientific	Cat# L3486
Low Density Lipoprotein from Human Plasma, oxidized (OxLDL)	Thermo Fisher Scientific	Cat# L34357
Critical Commercial Assays		
Click-iT Lipid Peroxidation Detection with Linoleamide Alkyne (LAA)	Thermo Fisher Scientific	Cat# C10446
Lipid Hydroperoxide (LPO) Assay Kit	Abcam	Cat# ab133085
PicoPure RNA Isolation kit	Thermo Fisher Scientific	Cat# KIT0204
Ovation RNA-seq v2 kit	NuGen	Cat# 7102-08
Ovation Rapid DR Multiplexing kit	NuGen	Cat# 0328
HiSeq 2500 Sequencing platform	Illumina	https://www.illumina.com/systems/sequencing-platforms/hiseq-2500.html
Deposited Data		
Mouse brain RNA-Seq transcriptome	(Zhang et al., 2014)	https://web.stanford.edu/group/barres_lab/brain_rnaseq.html
Astrocyte lipid droplet enrichment RNA-Seq	This paper	GEO: GSE128973
Experimental Models: Organisms/Strains		
Mouse: Emx1-cre	The Jackson Laboratory	RRID# IMSR_JAX:005628
Mouse: C57BL/6N	Charles River https://www.criver.com	N/A
Mouse: C57BL/6J	The Jackson Laboratory	N/A
Mouse: ApoE KO	The Jackson Laboratory	RRID# IMSR_JAX:002052
Rat: Sprague Dawley	Charles River https://www.criver.com	N/A
Recombinant DNA		
cDNA: ApoE-GFP	GenScript	N/A
Software and Algorithms		
(Fiji is just) ImageJ 2.0.0	NIH	https://imagej.nih.gov/ij/
Graphpad Prism 5	Graphpad	https://www.graphpad.com/
SPSS statistics 17.0	IBM Corporation	http://www.spss.com.hk/software/statistics/
Nikon Elements	Nikon Instruments	https://www.microscope.healthcare.nikon.com/products/software
ZEN Zeiss	Zeiss	https://www.zeiss.com/microscopy/int/products/microscope-software/zen.html
VAST Lite 1.2.01	(Kasthuri et al., 2015)	https://software.rc.fas.harvard.edu/lichtman/vast/
Bowtie2	(Langmead and Salzberg, 2012)	http://bowtie-bio.sourceforge.net/bowtie2/index.shtml
Cuffdiff	(Trapnell et al., 2010)	http://cole-trapnell-lab.github.io/cufflinks
Cutadapt	(Martin, 2011)	http://journal.embnet.org/index.php/embnetjournal/article/view/200
RSEM	(Li and Dewey, 2011)	http://deweylab.github.io/RSEM/

(Continued on next page)

Continued

REAGENT or RESOURCE	SOURCE	IDENTIFIER
TopHat	(Trapnell et al., 2009)	https://ccb.jhu.edu/software/tophat/manual.shtml
Cufflinks	(Trapnell et al., 2012)	http://cole-trapnell-lab.github.io/cufflinks/
Other		
Basal Medium Eagle (BME)	GIBCO	21010046
NbActiv4	BrainBits	Nb4-500
Antibiotic-Antimycotic	GIBCO	15240062
Fetal bovine serum	Thermo Fisher Scientific	10437-028
Sodium pyruvate	GIBCO	11360070
Glutamax	GIBCO	35050061
Poly-D-lysine Hydrobromide	Sigma-Aldrich	P6407
Papain Dissociation Enzyme	Worthington Biochemical	LK003176
VECTASHIELD HardSet Antifade Mounting Medium with DAPI	Vector Laboratories	H-1500

CONTACT FOR REAGENT AND RESOURCE SHARING

Further information and requests for resources and reagents should be directed to and will be fulfilled by the Lead Contact, Zhe Liu (liuz11@janelia.hhmi.org).

EXPERIMENTAL MODEL AND SUBJECT DETAILS

Animals

All animal work was approved by the Janelia Institutional Animal Care and Use Committee (IACUC 16–146). Sprague-Dawley timed pregnant rats were obtained from Charles River Laboratories and arrived at our facility one week prior to birth. P0-1 pups were used for primary neuron and astrocytes cultures. c57bl/6N mice were obtained from Charles River Laboratories and emx-cre, ApoE KO and c57bl/6J mice were obtained from Jackson Laboratory and bred at Janelia Research Campus. All experiments were performed on male animals. All mice were housed on a reverse 12-h light/12-h dark cycle; all experiments were performed during the dark cycle. No restrictions were imposed on food and water.

METHOD DETAILS

Primary culture of hippocampal neurons and astrocytes

Primary hippocampal neurons were prepared as previously described (Beaudoin et al., 2012). Briefly, the hippocampi were dissected from P0-P1 Sprague-Dawley rat, ApoE KO mouse or c57bl/6J mouse pups and digested with papain (Worthington Biochemical). After digestion, the tissues were gently triturated and filtered with the cell strainer. Neurons were grown on poly-D-lysine coated glass coverslips in NbActiv4 medium containing antibiotic-antimycotic at 37°C and used at DIV 5-7. Where specified 1 μm AraC was added to the media 2 days after plating and maintained for 4 days to prevent growth of astrocytes in neuronal cultures. Astrocyte cultures were grown in Basal Eagle Media containing 10% fetal bovine serum, 0.45% glucose, 1 mM sodium pyruvate, 2 mM glutamax supplement and antibiotic-antimycotic and used at DIV 3-5. For quantification, 5 images per coverslip were averaged.

Cloning ApoE-GFP

ApoE-GFP cDNA was synthesized and was subcloned into the AAV-CAG-WPRE vector using BamHI and HindIII restriction sites:
    GGATCCGCCACCATGAAGGTTCTGTGGGCTGCGTTGCTGGTCACATTCCTGGCAGGATGCCAGGCCAAGGTGGAGCAAGCGG
TGGAGACAGAGCCGGAGCCCGAGCTGCGCCAGCAGACCGAGTGGCAGAGCGGCCAGCGCTGGGAACTGGCACTGGGTCGCT
TTTGGGATTACCTGCGCTGGGTGCAGACACTGTCTGAGCAGGTGCAGGAGGAGCTGCTCAGCTCCCAGGTCACCCAGGAACTG
AGGGCGCTGATGGACGAGACCATGAAGGAGTTGAAGGCCTACAAATCGGAACTGGAGGAACAACTGACCCCGGTGGCGGAGGA
GACGCGGGCACGGCTGTCCAAGGAGCTGCAGGCGGCGCAGGCCCGGCTGGGCGCGGACATGGAGGACGTGTGCGGCCGCC
TGGTGCAGTACCGCGGCGAGGTGCAGGCCATGCTCGGCCAGAGCACCGAGGAGCTGCGGGTGCGCCTCGCCTCCCACCTGCG
CAAGCTGCGTAAGCGGCTCCTCCGCGATGCCGATGACCTGCAGAAGCGCCTGGCAGTGTACCAGGCCGGGGCCCGCGAGGGC
GCCGAGCGCGGCCTCAGCGCCATCCGCGAGCGCCTGGGGCCCCTGGTGGAACAGGGCCGCGTGCGGGCCGCCACTGTGGG
CTCCCTGGCCGGCCAGCCGCTACAGGAGCGGGCCCAGGCCTGGGGCGAGCGGCTGCGCGCGCGGATGGAGGAGATGGGCAG

CCGGACCCGCGACCGCCTGGACGAGGTGAAGGAGCAGGTGGCGGAGGTGCGCGCCAAGCTGGAGGAGCAGGCCCAGCAGAT
ACGCCTGCAGGCCGAGGCCTTCCAGGCCCGCCTCAAGAGCTGGTTCGAGCCCCTGGTGGAAGACATGCAGCGCCAGTGGGCC
GGGCTGGTGGAGAAGGTGCAGGCTGCCGTGGGCACCAGCGCCGCCCCTGTGCCCAGCGACAATCACACCGGTATGGTGAGCA
AGGGCGAGGAGCTGTTCACCGGGGTGGTGCCCATCCTGGTCGAGCTGGACGGCGACGTAAACGGCCACAAGTTCAGCGTGTCC
GGCGAGGGCGAGGGCGATGCCACCTACGGCAAGCTGACCCTGAAGTTCATCTGCACCACCGGCAAGCTGCCCGTGCCCTGGC
CCACCCTCGTGACCACCCTGACCTACGGCGTGCAGTGCTTCAGCCGCTACCCCGACCACATGAAGCAGCACGACTTCTTCAAGT
CCGCCATGCCCGAAGGCTACGTCCAGGAGCGCACCATCTTCTTCAAGGACGACGGCAACTACAAGACCCGCGCCGAGGTGAAG
TTCGAGGGCGACACCCTGGTGAACCGCATCGAGCTGAAGGGCATCGACTTCAAGGAGGACGGCAACATCCTGGGGCACAAGCT
GGAGTACAACTACAACAGCCACAACGTCTATATCATGGCCGACAAGCAGAAGAACGGCATCAAGGTGAACTTCAAGATCCGCCACA
ACATCGAGGACGGCAGCGTGCAGCTCGCCGACCACTACCAGCAGAACACCCCCATCGGCGACGGCCCCGTGCTGCTGCCCGAC
AACCACTACCTGAGCACCCAGTCCGCCCTGAGCAAAGACCCCAACGAGAAGCGCGATCACATGGTCCTGCTGGAGTTCGTGACC
GCCGCCGGGATCACTCTCGGCATGGACGAGCTGTACAAGTAAAAGCTT

Confocal and widefield imaging

All fixed cells and tissue were mounted in vectashield HardSet Antifade Mounting Medium with DAPI. Imaging was performed using the following microscopes: (1) Nikon Eclipse TiE inverted microscope equipped with a 20x objective lens (Nikon, N.A. = 0.75) and sCMOS camera (Zyla 4.2, Andor) and elements software. (2) Nikon spinning disk equipped with a 60x oil objective lens (Nikon, N.A. = 1.4) and EMCCD iXon Ultra Camera (Andor) and elements software. (3) Keyence BZ-X700 inverted microscope equipped with a 20x objective lens (Nikon, N.A. = 0.75) and 3CCD camera. (4) 880 Laser Scanning Confocal Microscope (LSM) equipped with a plan-aprochromat 63x oil objective (Zeiss, NA = 1.4) and 40x oil objective (Zeiss, NA = 1.2) and ZEN software (Zeiss).

Mitochondria fragmentation and surface area assay

Hippocampal neurons were treated with or without 500 μM NMDA in Nbactiv4 for 4 h, fixed with 4% PFA, immunostained for TOMM20 to label mitochondria and imaged using the Zeiss 880 LSM. Images of Tomm20 were blindly scored based on mitochondrial fragmentation. Cells were scored as either "fragmented" or "non-fragmented." The standard deviation was calculated based on the binomial distribution, sqrt(np(1-p)) where n is the number of cells and p the fraction of fragmented cells. For mitochondrial surface area, single confocal slices with the highest mitochondrial signal were used for quantification. Within ImageJ, a mask of the cell outline was made such that all pixels inside the neuron were equal to one and all pixels outside were null. Similarly, the mitochondria were thresholded such that all pixels inside the mitochondria were one and all pixels outside were null. The sum of all pixels was then measured for both images, essentially reporting the area occupied by either the total cell footprint or mitochondrial footprint. The ratio of the two is reported.

Autophagy induction assay

Hippocampal neurons were treated with or without 500 μM NMDA in Nbactiv4 for 4 h, fixed in ice-cold methanol, immunostained for LC3b to label autophagy and imaged using the Zeiss 880 LSM. Maximum intensity projections of three-dimensional image stacks of LC3b staining were first obtained. Then a series of image processing steps were performed to reduce background noise in order to automatically count LC3 positive puncta. Regions outside of the cell boundary were forced to null intensity to mediate false positive counts. Using a rolling ball radius of 5-20 pixels and sliding parabola the background of the image was then subtracted. Lastly, LC3 puncta were identified using the 3D Objects Counter (Bolte and Cordelières, 2006) and the number of puncta per cell are reported.

Lipid droplet assay

Hippocampal neurons or astrocytes washed in PBS and treated with or without the following drugs: 100 μM NMDA (500 μM NMDA if indicated on figure), 100 μM AP5, 100 μM glutamate, 250 nM Bafilomycin A1 (BAF), 100 μM Diethylumbelliferyl phosphate (DEUP), 10 mM 3-Methyladenine (3MA), 300 nM etoxomir, 5 μg/mL Low Density Lipoprotein (LDL), or 5 μg/mL oxidized Low Density Lipoprotein (oxLDL) in artificial cerebral spinal fluid (125 mM NaCl, 5 mM KCl, 2 mM MgSO$_4$, 24 mM NaHCO$_3$, 1.25 mM NaH2PO$_4$, 2 mM CaCl$_2$ pH 7.4) containing 10 mM glucose unless otherwise indicated, for 4 h at 37°C. Cells were washed 3 times in PBS, fixed in 4% PFA and stained with 1 μg/mL Nile Red or 5 μg/mL BODIPY 493/503 for 10 min at room temperature. Images for figures were taken using the Zeiss 880 LSM. Images for quantification were taken using the Nikon TiE widefield. Maximum intensity projections of three-dimensional image stacks of LD staining were first obtained. To remove background, a Gaussian blur was applied to a duplicate image and subtracted from the original image. The images were thresholded and particles were detected with a pixel size 2 to 100 and circularity from 0 to 1. For quantification, 10 images per coverslip were averaged.

Fatty acid and ApoE transfer assays

Neurons were incubated with NbActiv4 containing 2 μM BODIPY 558/568 C$_{12}$ (Red-C12) for 16 h. Neurons were washed three times in warm PBS and incubated for an additional 1 h in NbActiv4. Labeled neurons and unlabeled astrocytes on separate coverslips were washed twice with warm PBS and the coverslips were sandwiched together (facing each other) separated by paraffin wax and incubated in artificial cerebral spinal fluid (125 mM NaCl, 5 mM KCl, 2 mM MgSO$_4$, 24 mM NaHCO$_3$, 1.25 mM NaH2PO$_4$, 2 mM CaCl$_2$, 10 mM glucose pH 7.4) for 4 h at 37°C with or without 100 μM NMDA, 25 μM Pitstop2, 5 μg/mL Brefeldin A (BFA), 5 μg/mL Low Density

Lipoprotein (LDL), or 5 μg/mL oxidized Low Density Lipoprotein (oxLDL). To test ApoE transfer, neurons DIV2 were transduced with AAV2/1-CAG-ApoE-GFP-WPRE (MOI = 1.5 × 10^5) and maintained for 10 days before using in transfer assay. To test the effects of neuronal activity, neurons DIV2 were transduced with AAV2-hSyn-DIO-hM3Dq-mCherry and AAV-SL1-CAG-Cre (MOI = 1.5 × 10^5) and maintained for 10 days before using in transfer assay with or without 1 μM clozapine-N-oxide for 4 h. Cells were fixed and stained with BODIPY 493/503 to assess LDs in astrocytes and DAPI to assess cell death in neurons. Neurons expressing hM3Dq-mCherry were treated with or without 1 μM clozapine-N-oxide were fixed after 90 min and immunostained with anti-c-*fos* to confirm activation. Images for quantification were taken using the Nikon TiE widefield. Quantification of transfer was the same as LD assay.

Fatty acid pulse-chase assays
Astrocytes were incubated in complete media containing 2 μM BODIPY 558/568 C$_{12}$ (Red-C12) for 16 h. Astrocytes were washed three times in warm PBS and incubated for an additional 1 h in complete media and chased in aCSF with or without 100 μM NMDA. Astrocytes were fixed and mitochondria were immunolabelled with anti-Tomm20 to visualize mitochondria. Imaging was performed on the Zeiss 880 LSM. Quantification of transfer was the same as LD assay.

Lipoprotein particle depletion assay
Neurons were incubated with NbActiv4 containing 2 μM BODIPY 558/568 C$_{12}$ (Red-C12) for 16 h. Neurons were washed three times in warm PBS, incubated for an additional 1 h in NbActiv4 followed by 4 h in aCSF at 37°C. Neuron conditioned aCSF was collected and passed through a 0.2 μm filter, or centrifuged for 4,000 x g for 10 min, then 10,000 x g for 30 min then 250,000 x g for 2.5 hr at 4°C. Astrocytes were washed 3 times in PBS and incubated with deleted neuron-conditioned aCSF for 4 h in aCSF at 37°C, fixed, mounted, and imaged on the Zeiss 880 LSM. Quantification of transfer was the same as LD assay. Neuron-conditioned aCSF or aCSF containing 10 μM oleic-acid bound to albumin was centrifuged and analyzed by western blot. Samples were centrifuged for 4,000 x g for 10 min and 10 μl was analyzed as starting material. The supernatant was centrifuged at 10,000 x g for 30 min (low g) followed by 250,000 x g for 2.5 hr (high g) at 4°C and 10 μl of supernatants and pellets resuspended in 10 μl aCSF were analyzed by SDS-PAGE and western blotting. Oleic-acid bound to albumin was analyzed by Coomassie blue stain.

Lipid peroxidation and ROS assays
For lipid hydroperoxide assay, neurons were grown on PDL-coated plastic dishes. Neurons were incubated in HBSS containing 2 mM calcium with or without 100 μM NMDA for 6 h. Neuron-conditioned medium was collected and lipid hydroperoxides were extracted and analyzed using a lipid hydroperoxide assay kit according to the manufacturers protocol. For Click-iT lipid peroxidation assay, neurons were treated for 4 h in NbActiv4 with or without 500 μM NMDA with 50 mM linoleamide alkyne added for the last 2 h. Cells were washed three times in PBS, fixed in 4% paraformaldehyde for 10 min and blocked in 1% BSA containing 0.2% Triton X-100 for 30 min. Cells were incubated in the Click-iT reaction cocktail for 30 min at room temperature, washed twice with 1% BSA, twice with PBS, mounted and imaged using the Zeiss 880 LSM. Mean intensities and integrated density for each thresholded cell were measured using ImageJ. Quantification of transfer was the same as LD assay. For quantification, 8 images per coverslip were averaged. For CellRox assay, astrocytes were treated for 4 h in aCSF with or without 100 μM NMDA with 5 μM CellROX Green added for the last 30 min. Cells were washed three times with PBS and fixed with 3% PFA for 10 min and mounted. Imaging was performed on a Nikon Eclipse TiE Inverted microscope equipped with a 60X Oil-immersion objective lens (Nikon, N.A. = 1.4) and EMCCD camera (iXon Ultra 897, Andor). Images were shade corrected and mean intensities and integrated density for each thresholded nuclei were measured using ImageJ. For quantification, 10 images per coverslip were averaged. For BODIPY 581/591 C11 lipid peroxidation assay, astrocytes were incubated in HBSS with or without 100 μM NMDA or 50 μM α-tocopherol for 4 h with 2 μM BODIPY 581/591 C11 added for the last 30 min and 1 h for astrocytes and neurons, respectively. Cells were then washed with HBSS and imaged live in HBSS with or without NMDA using the Nikon spinning disk confocal microscope and Zeiss LSM 880 for astrocytes and neurons, respectively. Z stacks were taken at both green and red channels. Relative lipid peroxidation was indicated by the ratio of green fluorescence intensity over red fluorescence intensity from background subtracted images using imageJ.

Electron microscopy of purified particles
Primary hippocampal neurons were plated on 10-cm PDL-coated culture plates. 1 μm AraC was added to the media 2 days after plating and maintained for 4 days to prevent growth of astrocytes in neuronal cultures. Neurons were incubated with 5 mL culture media for 18 h. Neuron-conditioned media was centrifuged at 10,000 x g for 20 min to remove cell debris and dead cells. Supernatant was centrifuged at 300,000 x g for 3 h and the pellet was resuspended in 15 μl of PBS. For negative staining, 5 μl drops of this suspension were adsorbed onto glow-discharged copper grids coated with Formvar-carbon and stained with 1% uranyl acetate in water. Samples were imaged in a Tecnai Spirit electron microscope (FEI, Hillsboro, OR) operating at 80 kV equipped with an Ultrascan 4000 digital camera (Gatan Inc, CA).

Mouse brain sample preparation for FIB-SEM
2-month old male C57/BL6 mouse was deeply anesthetized and transcardially perfused with 30 mL of 3% PFA (60 mM NaCl, 130 mM glycerol, 10 mM sodium phosphate buffer). The brain was carefully dissected out from the skull and postfixed with 50 mL of 3% PFA (30 mM of NaCl, 70 mM glycerol, 30 mM PIPES buffer, 10 mM betaine, 2 mM CaCl2, 2 mM MgSO4) under room temperature for 2 h.

The brain sample was then rinsed in a 400 mOsM buffer (65 mM NaCl, 100 mM glycerol, 30 mM PIPES buffer, 10 mM betaine, 2 mM CaCl2, and 2 mM MgSO4) for half an hour, followed by vibratome sectioning (coronal sections, 100 μm thickness) using a Leica VT1000S vibratome in the same buffer. 100 μm sections were then fixed in 1% PFA, 2% glutaraldehyde solution (30 mM NaCl, 70 mM glycerol, 30 mM PIPES buffer, 10 mM betaine, 2 mM CaCl2, 2 mM MgSO4, 75 mM sucrose) overnight at 4°C. Sections were then washed using the 400 mOsM rinsing buffer (see above). Round samples of the hippocampus were created from the 100 μm coronal sections using a 2 mm biopsy punch (Miltex). The 2 mm samples were dipped in hexadecene, placed in 100 μm aluminum carrier, covered with a flat carrier and high-pressure frozen using a Wohlwend compact 01 High pressure freezer. Samples were then freeze-substituted in 0.5% osmium tetroxide, 20 mM 3-Amino-1,2,4-triazole, 0.1% uranyl acetate, 4% water in acetone, using a Leica AFS2 system. Specimens were further dehydrated in 100% acetone and embedded in Durcupan resin.

FIB-SEM imaging of mouse brain sample

Durcupan embedded mouse hippocampus CA1 sample was first mounted on a Cu stud, then imaged by a customized Zeiss Merlin FIB-SEM system previously described (Xu, C. S. et. al. Enhanced FIB-SEM. Systems for Large-Volume 3D Imaging, eLife 2017 May; https://doi.org/10.7554/eLife.25916). The block face was imaged by a 2 nA electron beam with 1.2 keV landing energy at 2 MHz. The x-y pixel resolution was set at 8 nm. A subsequently applied focused Ga+ beam of 15 nA at 30 keV strafed across the top surface and ablated away 4 nm of the surface. The newly exposed surface was then imaged again. The ablation – imaging cycle continued about once every minute for one week. The sequence of acquired images formed a raw imaged volume, followed by post processing of image registration and alignment using a Scale Invariant Feature Transform (SIFT) based algorithm. The aligned stack was binned by a factor of 2 along z to form a final isotropic volume of $60 \times 80 \times 45$ μm^3 with $8 \times 8 \times 8$ nm^3 voxels, which can be viewed at any arbitrary orientations.

Cell Sorting and RNA-seq library preparation

Primary hippocampal astrocytes (DIV 4) were incubated for 10 min in 1 ng/mL Nile Red in PBS at 37°C, trypsinized to detach from the cultured cells, spun at 250 x g for 5 min, re-suspended in PBS and passed through a cell strainer to yield single cells. Cells were sorted for on the BD FACS ARIA II using the 488 nm laser to separate LD positive and negative cells. Unstained cells were used as a negative control to establish the gates and exclude dead cells and doublets. Sorted astrocytes were lysed in PicoPure extraction buffer. RNA extraction and RNA library preparation was performed as described in (Cembrowski et al., 2016). Briefly, RNA was extracted using PicoPure RNA Isolation kit, cDNA was amplified using Ovation RNA-seq v2 kit and the Ovation Rapid DR Multiplexing kit was used to make the sequencing library. Libraries were sequenced on the HiSeq 2500 platform with single-end 100 bp reads. Reads were first trimmed using cutadapt (Martin, 2011), then aligned to the rn6 transcriptome (GCF_000001895.5) using RSEM (Li and Dewey, 2011). Gene expression estimates were reported as Fragments Per Kilobase of transcript per Million mapped reads (FPKM).

Gene expression level testing and gene ontology analysis

We mapped sequencing data back to the rat reference genome (Rt6) by Bowtie2 (Langmead and Salzberg, 2012). Transcript isoforms were reconstructed from PE reads using TopHat (Trapnell et al., 2009) and abundances estimated using Cufflinks (Trapnell et al., 2012). Read counts were tallied for each Ensembl annotated protein-coding gene incremented by 1 and differential expression tested using Cuffdiff using all qualified samples. Gene Ontology analysis was performed separately on upregulated and downregulated genes using DAVID Bioinformatics Functional Annotation Tool (Huang et al., 2007a, 2007b). Cell-type specific mouse mRNA seq data for astrocyte, neuron, oligodendrocyte progenitor cells, newly formed oligodendrocytes, myelinating oligodendrocytes, microglia, and endothelial cells were obtained from (Zhang et al., 2014). Cross-species relative gene expression levels were calculated by direct normalization of FPKM of homologous genes.

Pial strip devascularization and chemogenetic stimulations

All procedures were conducted in accordance with protocols approved by the Janelia Institutional Animal Care. Pial strip devascularization was performed as previously described (Farr and Whishaw, 2002). Adult C57BL6 mice were anaesthetized with isoflurane and buprenorphine (0.1 mg/kg, SC) was administered as an analgesic. A craniometry was performed over the motor cortex. The coordinates of the square incised measured from Bregma; (a) A 1.0 mm, L 1.0 mm (b) A 1.0 mm, L 2.0 mm (c) A 2.0 mm, L 2.0 mm (d) A 2.0 mm, L 1.0 mm. The dura mater was cut and peeled away using the sharp edge of a sterile hypodermic needle and fine forceps. Sterile saline-soaked absorption spears were used to wipe away the pia and superficial vasculature, the area was flushed with ample sterile saline and gelfoam was applied to the stroke region which aids in coagulation. A thin layer of artificial dura and bone wax was applied to protect the exposed tissue and the wound was closed with stitches and vetbond. Marcaine was applied to the incision site and ketoprofen (5 mg/kg) was administered at the end of the surgery and once per day for 2 days after surgery. For *in vivo* chemogenetic stimulation, mice were anesthetized with isoflurane and a small craniotomy (0.1 mm x 0.1 mm) was performed over the motor cortex for the insertion of the injection needle. Emx1-cre mice were injected with 200 nL of AAV2.1-hSyn-DIO-hM3Dq-mCherry and C57BL6 mice were co-injected with AAV2-hCamKII-DIO-hM3Dq-2A-mCherry or AAV2.1-hSyn-DIO-hM3Dq-mCherry plus 200 nL AAV-SL1-hSyn-cre into the motor cortex (coordinates A/P: 1.0 mm, M/L: 1.5 mm, D/V: 0.5 mm). All virus titers were 10^{13} GC/mL. Marcaine was applied to the incision site and ketoprofen (1 mg/kg) was administered at the end of the surgery and once per day

for 2 days after surgery. 4 weeks post-injection, mice were injected with clozapine-N-oxide (5 mg/kg) or saline intraperitoneally, twice a day for three days. For quantification, 3-5 images per hemisphere or treatment were averaged

Histology

Mice were deeply anesthetized with isoflurane and intracardially perfused with 4% paraformaldehyde in phosphate-buffered saline. The brains were removed and post-fixed in 4% PFA overnight at 4°C. Serial 70 μm sections spanning the lesion or injection site were obtained on a vibratome. Slices were incubated at room temperature for 1 h in blocking buffer (PBS, 2% BSA, 0.2% Triton X-100), overnight in primary antibody in blocking buffer and 4 h in secondary antibody plus BODIPY-493/503 in blocking buffer. Between antibodies, slices were washed 3 times with PBS containing 0.2% Triton X-100. Imaging was performed using the Nikon TiE and Keyence for whole brain imaging and stitching. Cell type and subcellular imaging was performed using the Zeiss 880 LSM.

QUANTIFICATION AND STATISTICAL ANALYSIS

Statistical analysis was performed using Graphpad Prism 5 and SPSS Statistics 17.0. Statistical significance was determined by two-tailed Student's t test for comparison of two groups or by one-way ANOVA with post hoc Tukey test for multiple comparisons. Where control groups were normalized to 1, a one-sample t test was employed. The number of technical and experimental replicates can be found in the figure legends for each experiment. p value are listed on the figures.

DATA AND SOFTWARE AVAILABILITY

Raw RNA-seq datasets were deposited in the National Center for Biotechnology Information (NCBI) Gene Expression Omnibus under GEO: GSE128973. Enriched genes and gene ontology pathways can be found in Table S1.
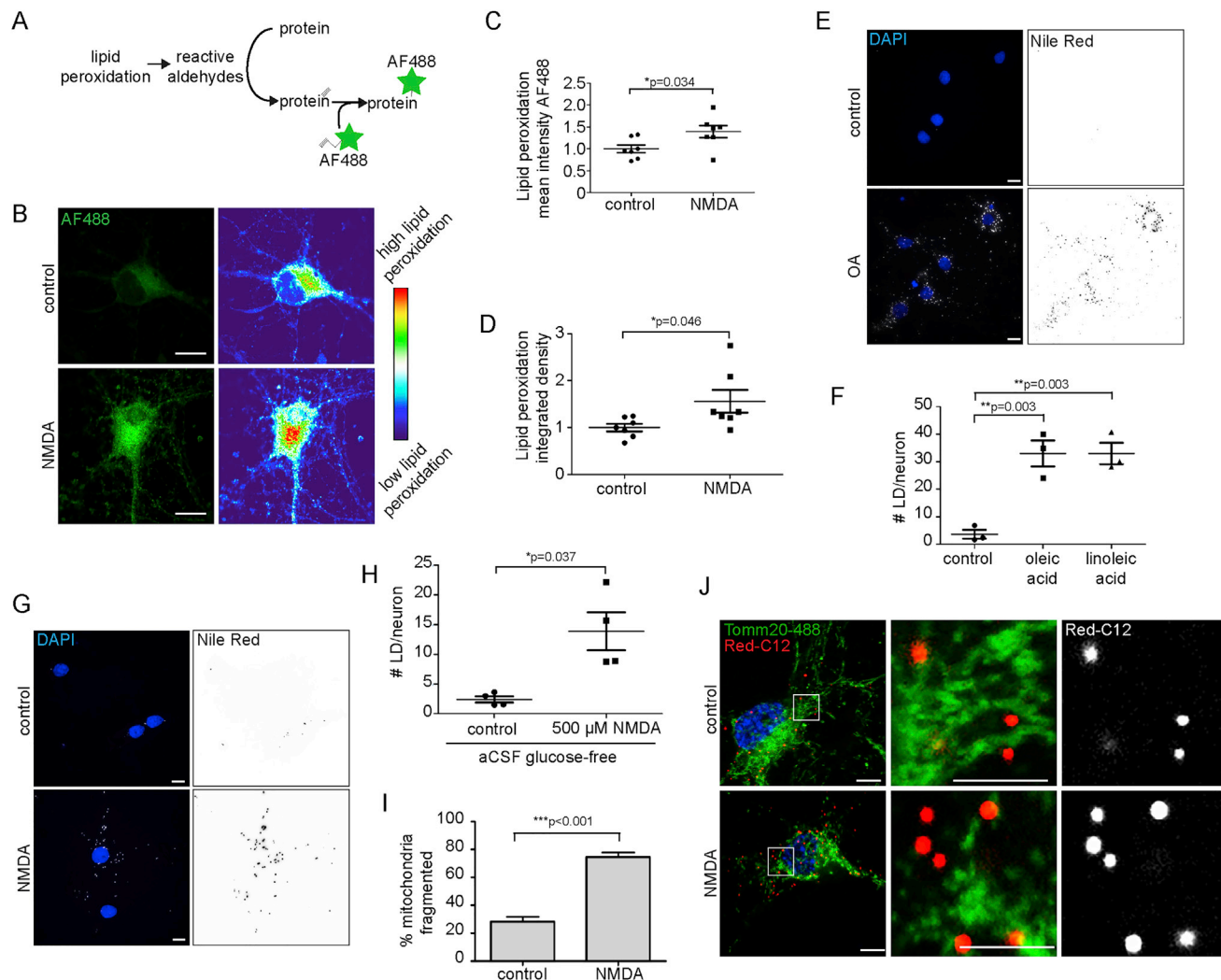
Figure S1. Excitotoxicity-Induced Lipid Droplets and Mitochondrial Dysfunction in Neurons, Related to Figure 1

(A) Schematic of Click-iT lipid peroxidation assay.

(B-D) Cropped confocal image of neurons ± NMDA were assayed for lipid peroxidation. Mean intensity and integrated density were quantified. 3 independent experiments; n = 7 coverslips/treatment; 17.2 ± 5.4 cells cells/coverslip; mean ± SEM.

(E-F) Neurons ± oleic acid (OA) or linoleic acid (LA) were fixed and stained with Nile Red, and the number of LDs was quantified. Left panel: Cropped widefield images of LDs displayed as maximum intensity projection on top of single DAPI image. Right panel: Inverted maximum intensity projection of LDs. 3 independent experiments; n = 4 coverslips/treatment; 43.2 ± 12.5 cells/coverslip; mean ± SEM.

(G-H) Neurons ± NMDA in glucose-free aCSF were fixed and stained with Nile Red, and the number of LDs was quantified. Left panel: Cropped widefield images of LDs displayed as maximum intensity projection on top of single DAPI image. Right panel: Inverted maximum intensity projection of LDs. 3 independent experiments; n = 4 coverslips/treatment; 45.2 ± 11.2 cells/coverslip; mean ± SEM.

(I) Quantification of Figure 1J. Neurons were scored blind as having normal or fragmented mitochondria. 2 independent experiments; n = 60 cells/treatment; mean ± SD.

(J) Cropped confocal images of neurons were loaded with Red-C12 overnight, chased in ± 500 μM NMDA, fixed and immunostained for TOMM20. Boxed area magnified on right.

All images are maximum intensity projections. Scale bars are 10 μm.
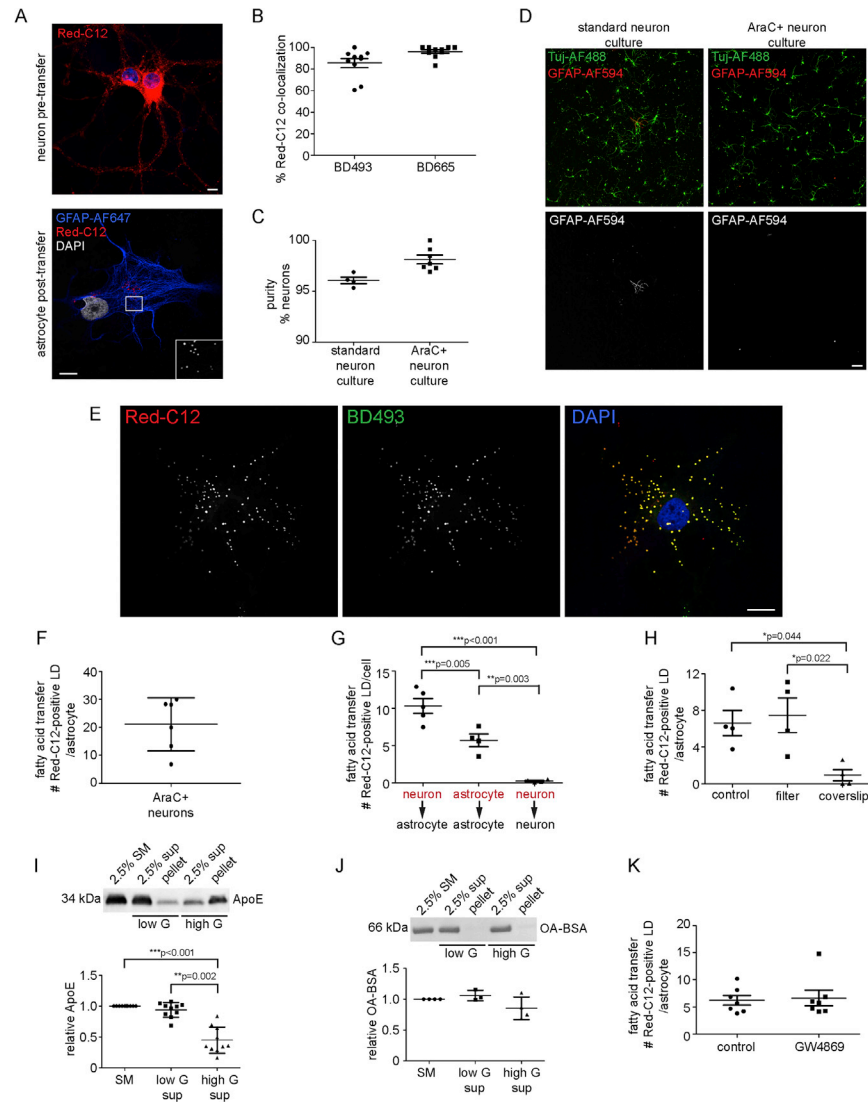
Figure S2. Specificity of FA Transfer from Neurons to Astrocytes, Related to Figure 2

(A) Top panel: Confocal image of neurons pre-transfer labeled with Red-C12. Bottom panel: Cropped confocal image of astrocytes post-transfer assay were immunostained for GFAP and analyzed for the appearance of Red-C12-positive LDs. Boxed area shows zoom of Red-C12. Scale bars, 10 μm.

(B) Percentage of astrocytic LDs stained with BD493 or BD665 containing Red-C12 following transfer assay. 2 independent experiments; n = 10 cells/treatment; mean ± SD.

(C-D) Neuronal cultures ± AraC were immunostained for Tuj1 and GFAP to label neurons and astrocytes, respectively. Tiled confocal images were stitched using 10% overlap. Scale bars, 100 μm. 2 (without AraC) and 3 (with AraC) independent experiments; minimum of n = 4 coverslips/treatment; 205.5 ± 134.4 cells/coverslip; mean ± SEM.

(E-F) Cropped confocal image of astrocytes post-transfer assay using neurons treated with AraC. Cells were fixed and stained with BD493. Scale bars, 10 μm. Quantification of Red-C12-positive LDs. 3 independent experiments; n = 6 coverslips; 28.0 ± 6.1 cells/coverslip; mean ± SEM.

(G) Quantification of Red-C12-positive LDs following transfer assay between different cell types. Donor cells pre-incubated with Red-C12 are in red. 3 independent experiments; minimum n = 4 coverslips/treatment; 30.2+/−7.4 cells/coverslip; mean ± SEM.

(H) Quantification of Red-C12-positive LDs in astrocytes following transfer assay using conditioned aCSF from empty coverslips preloaded with Red-C12 or neuron-conditioned media filtered through a 0.2 μm pore. 2 independent experiments; minimum of n = 4 coverslips/treatment; 22.9 ± 1.7 cells/coverslip; mean ± SEM.

(I) Neuron-conditioned media following centrifugation assay described in Figure 2D was analyzed by western blot using anti-ApoE. Four independent experiments; n = 10; mean ± SD.

(J) Ponceau-S stain of oleic-acid bound to albumin (OA-BSA) in aCSF following centrifugation assay described in Figure 2D. 3 independent experiments; minimum of n = 3; mean ± SD.

(K) Quantification of Red-C12-positive LDs in astrocytes following transfer assay ± GW4869. 3 independent experiments; n = 7 coverslips/treatment. 32.4 ± 7.4 cells/coverslip; mean ± SEM.

A

B

D

C

E

F

G
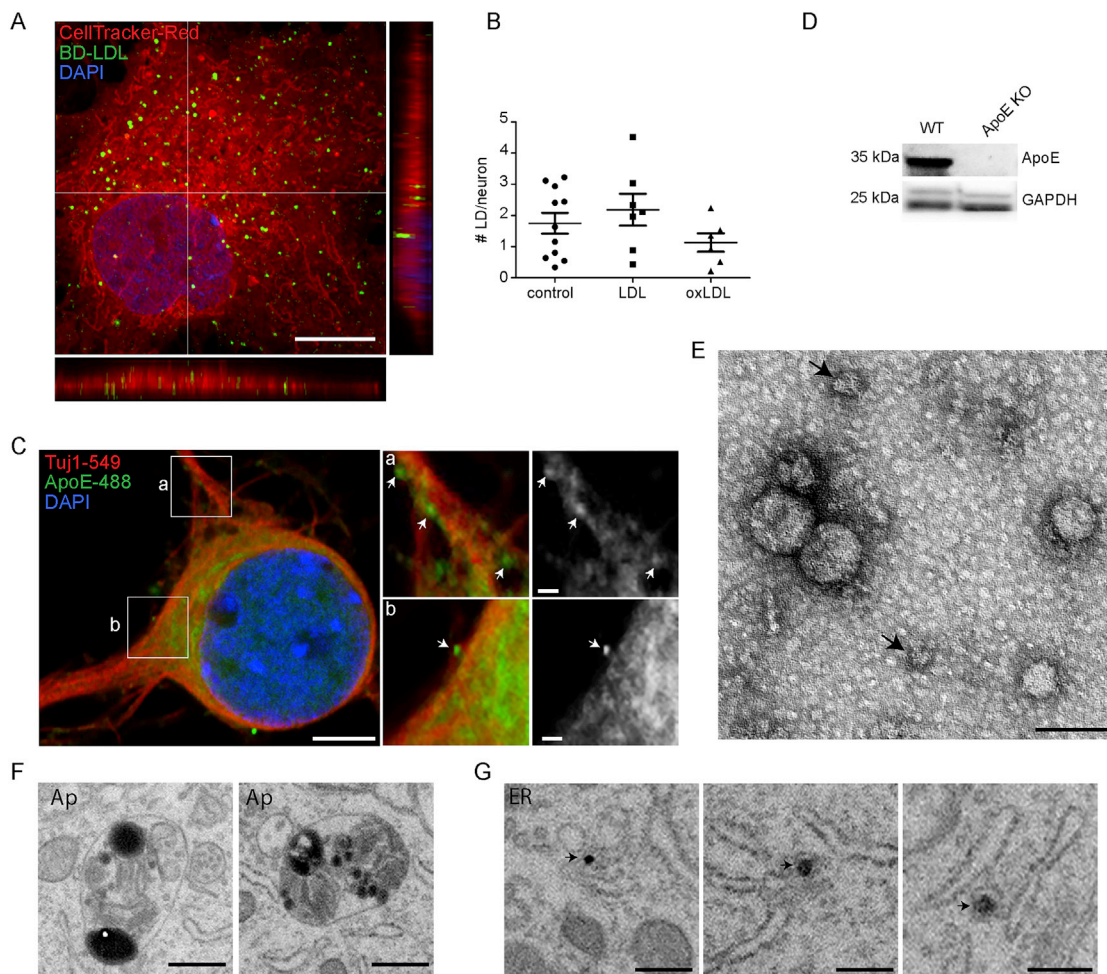
Figure S3. ApoE-Positive Lipid Particles Are Synthesized in Neurons, Related to Figure 3

(A) Cropped confocal image of astrocyte treated with BD515-labeled LDL (BD-LDL) and labeled with CellTracker Red. Right and bottom panels show orthogonal view of 0.5 μm sections. Scale bar, 10 μm.

(B) Neurons ± LDL or oxLDL were fixed and stained with BD493, and the number of LDs was quantified. 3 independent experiments; minimum of n = 6 coverslips/treatment; 27.1 ± 5.8 cells/coverslip; mean ± SEM.

(C) Cropped confocal image of neurons immunostained for ApoE and Tuj1. Boxed areas magnified in right panels. Arrows highlight ApoE-positive puncta. Scale bars are 5 μm and 0.5 μm.

(D) Hippocampal cells from wild-type (WT) and ApoE knockout (KO) mice were analyzed by western blot.

(E) Electron micrograph of particles purified from neuron-conditioned media observed by negative staining. Scale bars are 50 nm. Arrows indicate potential lipid particles smaller than 25 nm.

(F-G) Pyramidal neuron from area CA1 in hippocampus was imaged by focused ion beam scanning electron microscopy. Ap denotes autophagosomes/autolysosome. Arrows shows nascent lipid particle in ER. Scale bars are 500 nm.

A

B
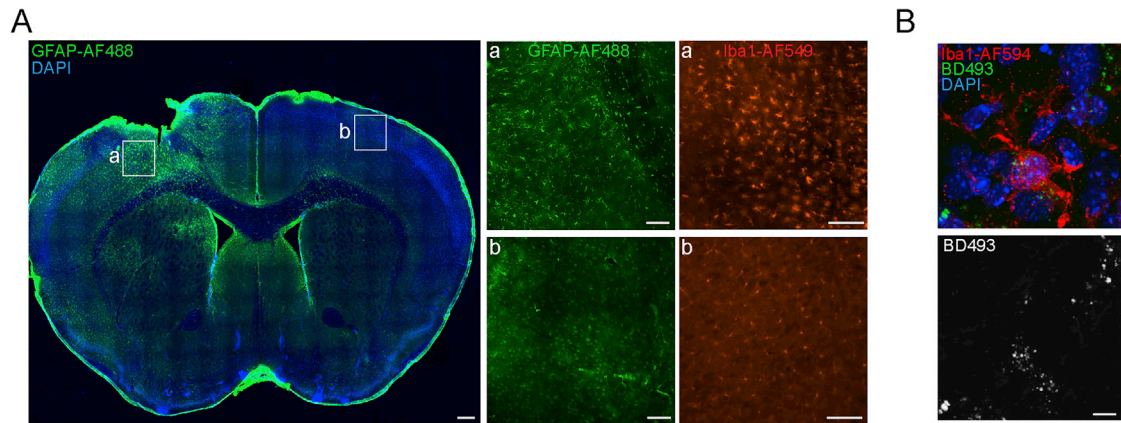
Figure S4. Pial Strip Lesion Induces Oxidative Injury, Related to Figure 4

(A) Mouse brain post pial strip lesion was immunostained for GFAP and Iba1 to label astrocytes and microglia, respectively. Tiled widefield images were stitched with 10% overlap. Scale bars are 100 nm.

(B) Mouse cortex post pial strip lesion was immunostained for anti-Iba1 and stained with BD493. Maximum intensity projections of confocal images are displayed. Scale bars are 10 μm.
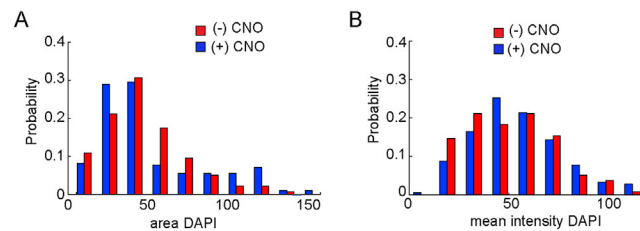
Figure S5. Neuronal Nuclei Are Unaffected following Stimulation with CNO, Related to Figure 5
(A-B) FA transfer assay using neurons expressing hM3Dq-mCh with or without CNO. Neurons were fixed, stained with DAPI and nuclei area and mean intensity were quantified and displayed as probability histograms. 3 independent experiments; n = 137 and 183 cells for control and CNO treatments, respectively.
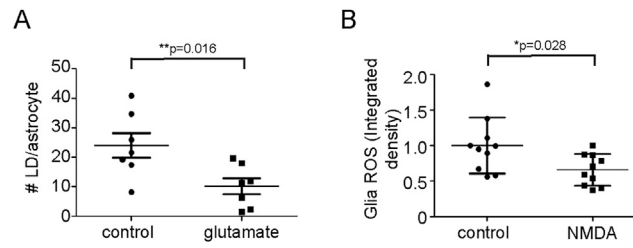
Figure S6. Glutamate-Induced Reduction in Astrocytic LDs, Related to Figure 6

(A) Astrocytes ± glutamate were fixed and stained with Nile Red, and the number of LDs was quantified. 3 independent experiments; n = 6 coverslips/treatment 24.6 ± 3.7 cells/coverslip; mean ± SEM.

(B) Quantification of integrated density of CellRox in astrocytes ± NMDA of Figure 6I. 4 independent experiments; n = 7 coverslips/treatment; 29.5 ± 5.2 cells/coverslip; mean ± SEM.
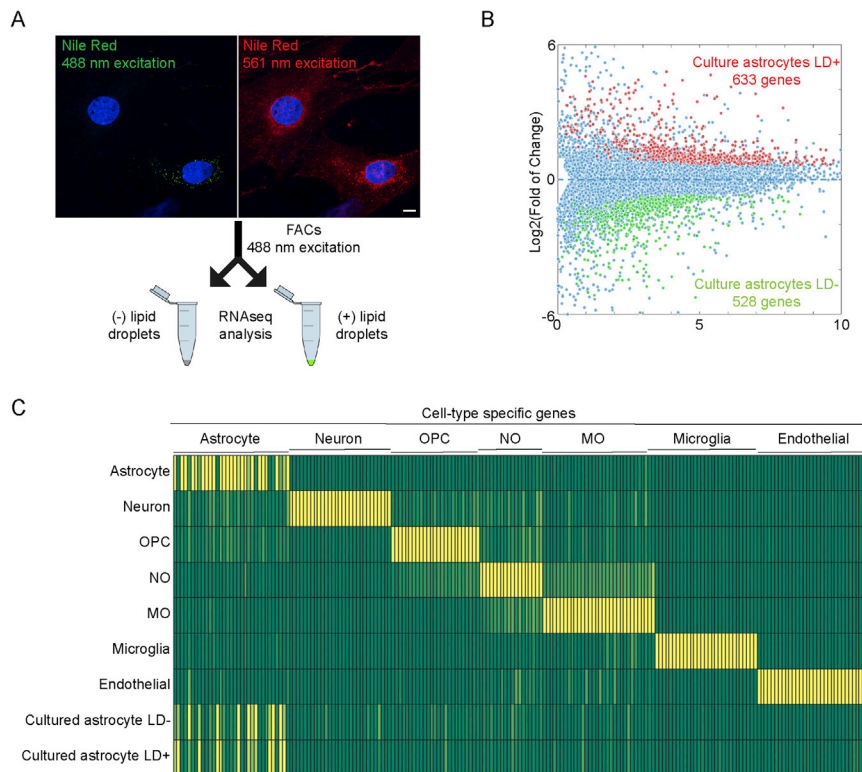
Figure S7. Differential Gene Expression in Astrocytes Containing LDs, Related to Figure 7

(A) Schematic of cell sorting and RNA-seq workflow. Cropped confocal image of cultured astrocyte stained with Nile Red and imaged using 488 nm and 561 nm excitation. Scale bars are 10 μm. Cells were separated by FACS using 488 nm excitation and analyzed by mRNA-seq.

(B) Folds of changes (y; Log2 scale) and average gene expression levels (x; FPKM) for all tested genes for cultured astrocytes with and without LDs (4 mRNA-seq replicates). Right Panel: Selected genes upregulated in astrocytes containing LDs.

(C) Astrocytes enriched for astrocyte-specific genes. Average gene expression levels for cell-type specific markers (see Table S1) were normalized to cell-type specific mRNaseq data published in (Zhang et al., 2014). The highest gene expression level is set as 1 and relative gene expression levels for all genes are calculated and plotted accordingly. OPC, NO and MO are short for oligodendrocyte progenitor cells, newly formed oligodendrocytes and myelinating oligodendrocytes, respectively.